Joule

CellPress

Article

Alkaline Quinone Flow Battery with Long Lifetime at pH 12

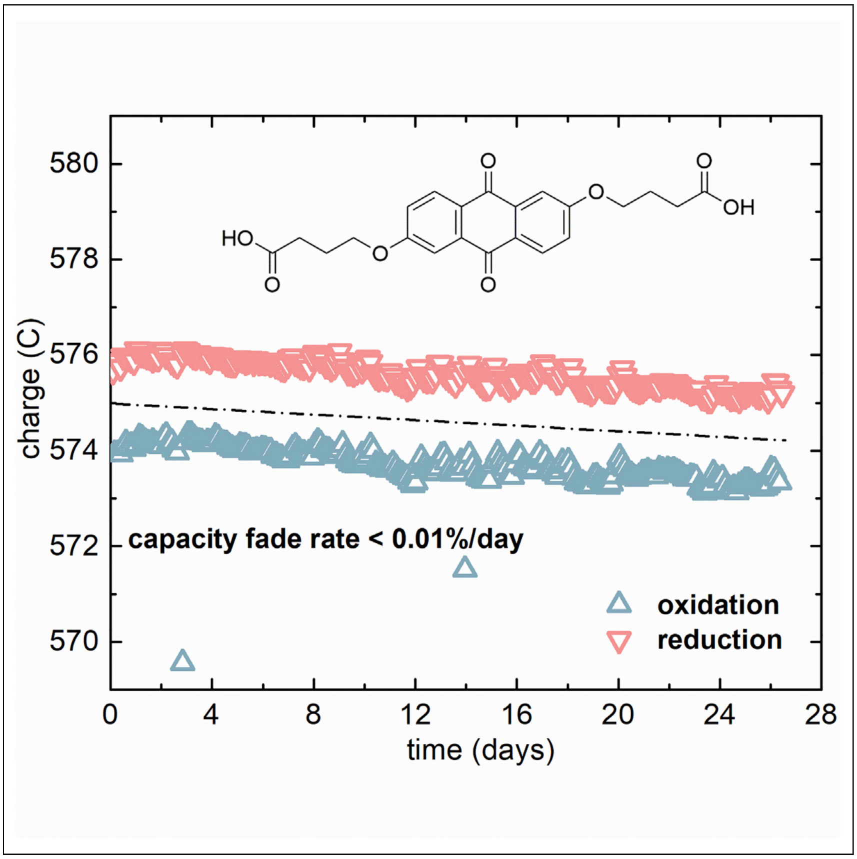

This work demonstrates a new, organic redox-flow battery (RFB) that outlives its predecessors, offering the longest-lived high-performance organic flow battery to date. It appears to be the first aqueous-soluble organic RFB chemistry to meet all the technical criteria for commercialization. The potential low reactant and membrane costs of this chemistry offer the potential for RFBs of this type to be used cost effectively at the gigawatt scale in order to enable massive penetration of intermittent renewable electricity.

David G. Kwabi, Kaixiang Lin, Yunlong Ji, ..., Alán Aspuru-Guzik, Roy G. Gordon, Michael J. Aziz

maziz@harvard.edu

HIGHLIGHTS

Near-neutral chemistry for rechargeable, aqueous-soluble, organic redox-flow batteries

Capacity fade rate of ~0.01%/day, the longest lifetime for a quinone-based electrolyte

Meets technical criteria for commercialization of redox-flow batteries

Kwabi et al., Joule *2*, 1894–1906
September 19, 2018

https://doi.org/10.1016/j.joule.2018.07.005

Joule

CellPress

Article

Alkaline Quinone Flow Battery with Long Lifetime at pH 12

David G. Kwabi,[1,4] Kaixiang Lin,[2,4] Yunlong Ji,[2] Emily F. Kerr,[2] Marc-Antoni Goulet,[1] Diana De Porcellinis,[1] Daniel P. Tabor,[2] Daniel A. Pollack,[3] Alán Aspuru-Guzik,[2] Roy G. Gordon,[1,2] and Michael J. Aziz[1,5,*]

SUMMARY

We demonstrate a long-lifetime, aqueous redox-flow battery that can operate at a pH as low as 12 while maintaining an open-circuit voltage of over 1 V. We functionalized 2,6-dihydroxyanthraquinone (2,6-DHAQ) with highly alkali-soluble carboxylate terminal groups. The resulting negative electrolyte material 4,4′-((9,10-anthraquinone-2,6-diyl)dioxy)dibutyrate (2,6-DBEAQ) was six times more soluble than 2,6-DHAQ at pH 12. Symmetric cell cycling with 2,6-DBEAQ on both sides of the cell demonstrates a capacity fade rate of <0.01%/day and <0.001%/cycle. By pairing 2,6-DBEAQ with a potassium ferri-/ferrocyanide positive electrolyte and utilizing a non-fluorinated membrane, this near-neutral flow battery shows a capacity fade rate that is the lowest of any quinone and rivals the lowest ever reported for any flow battery in the absence of rebalancing processes. This result adds the important attribute of long calendar life to quinone-based redox-flow batteries, which may enable massive penetration of intermittent renewable electricity.

INTRODUCTION

The cost of wind and photovoltaic electricity has dropped so much that one of the greatest technical barriers to their widespread substitution for fossil electricity is their intermittency. Cost-effective, safe, and scalable stationary electricity storage could solve this problem. Traditional enclosed batteries such as lithium ion batteries are common, but they cannot cost effectively store enough energy for the long discharge durations at rated power that appear to be necessary for regulating the intermittency of renewables. Redox-flow batteries (RFBs) comprise one class of energy storage systems particularly suited for long-duration discharge because energy-storing species are held in liquid form in external tanks that are separated from the power generation stack. Consequently, energy and power ratings can be scaled independently, and discharge durations (energy:power ratios) of several hours to days can be achieved at the rated power.

The RFBs farthest along the commercial pathway are based on charge storage of vanadium ions in acidic electrolytes, but they have limited potential for widespread adoption due to the high cost and low earth abundance of vanadium.[1] As a consequence, RFBs based on redox-active organic and organometallic reactants[2–6] are receiving much research interest, as they are potentially much less expensive than their vanadium-based counterparts; in addition, organic reactants can be chemically modified through selective functionalization in order to improve aspects of performance such as voltage, rate capability, and energy density.

Context & Scale

Electricity generation from renewable sources such as solar and wind can eliminate fossil-fuel-based systems if their intermittent output can be regulated using safe, cost-effective energy storage. Aqueous-soluble organic redox-flow batteries (RFBs) are a potentially safer, less expensive alternative to lithium ion batteries and vanadium flow batteries for long-discharge duration storage. We demonstrate a long-lifetime, organic-molecule-based RFB that can operate in weak alkaline conditions while maintaining an open-circuit voltage of over 1 V. The negative electrolyte comprises an anthraquinone functionalized with solubilizing carboxylate groups and the positive electrolyte comprises the food additive potassium ferrocyanide. The RFB can operate with an inexpensive membrane and shows a capacity fade rate that rivals the lowest ever reported for any RFB in the absence of rebalancing processes. This result adds the important attribute of long calendar life to quinone-based RFBs.

One drawback of many reported organic RFBs, however, is their low chemical stability because organic molecules are susceptible to degradation reactions such as nucleophilic substitution, gem-diol formation, and self-polymerization. Several organic and organometallic RFBs have been reported in the past 5 years, operating in highly acidic, highly alkaline, or neutral conditions, based on quinone,[2,4,7] viologen,[8–11] ferrocene,[8] alloxazine,[5] and nitroxide radical[10,12–14] motifs. Most of them, however, experience high temporal capacity fade rates of 0.1%–3.5%/day, which limits their long-term use over many years. Such relatively short lifetimes render most of these chemistries unsuitable for commercialization, while motivating further research into the development of organic molecules with high stability in both oxidized and reduced redox states.

Here, we report a new negative electrolyte (negolyte) molecule synthesized from our previously reported DHAQ chemistry that exhibits record high chemical stability, leading to the lowest temporal capacity fade among quinone-based flow batteries, on the order of ~5%/year. This is among the lowest reported for any RFB in the absence of rebalancing procedures. The approach involves the introduction of ether-linked alkyl chains with solubilizing carboxylate functional groups onto an anthraquinone core and affords high chemical stability and high solubility (0.6 M at pH 12; 1.1 M at pH 14) in alkaline electrolyte (Table S1). We hypothesized that solubility would be enhanced by frustrating crystallization if we attached solubilizing groups via short hydrophobic chains that were not so long that their hydrophobicity dominates. The solubility enhancement reduces the concentration of supporting electrolyte by two orders of magnitude without compromising the ionic conductivity of the system. Pairing 2,6-DBEAQ with a ferro-/ferricyanide-based positive electrolyte (posolyte) results in a battery with an open-circuit voltage of 1.05 V and theoretical volumetric energy density of ~12 Wh/L at pH 14 and ~17 Wh/L at pH 12 (Table S2). We further show that this *O*-alkylated anthraquinone can be used in a flow battery at pH 12 with an inexpensive hydrocarbon-based membrane that features exceptionally high permselectivity and low permeability of both the alkylated anthraquinone and ferricyanide species, affording century-scale timescales for reactant crossover. These results highlight the importance of synthetic approaches to increase the chemical stability of active species and constitute a leap forward in realizing high-performance aqueous organic RFBs that exhibit long cycle and calendar life at low capital cost.

RESULTS AND DISCUSSION

Synthesis and Cyclic Voltammetry Study

Figure 1 illustrates the synthetic route, chemical structures, and cyclic voltammograms (CVs) of various isomers of DBEAQ. All DBEAQ isomers can be synthesized fairly simply by an *O*-alkylation reaction followed by hydrolysis of the ester to afford the highly alkali-soluble carboxylic acid terminal groups (Figure 1A). Since the second hydrolysis reaction is almost 100% in yield and the by-product is a volatile organic, i.e., methanol, we expect that for the industrial process, the negolyte can be prepared directly after the hydrolysis step and the removal of methanol without the additional cost incurred by two unnecessary acid-base treatments, namely, collection of the hydrolyzed DBEAQ product via acidification for characterization and deprotonation of DBEAQ with a designated amount of base for electrolyte preparation.

After the functionalization, the resulting DBEAQ isomers (Figures 1B and S1–S3) showed a significant improvement in solubility versus their hydroxyl counterparts at both pH 14 and pH 12. For instance, the room-temperature solubility of 2,6-DBEAQ exceeded 1 M in pH 14 and 0.5 M in pH 12 KOH solution (Table S1), as opposed to 0.6 M[4] and 0.1 M,

[1]Harvard School of Engineering and Applied Sciences, Cambridge, MA 02138, USA

[2]Department of Chemistry and Chemical Biology, Harvard University, Cambridge, MA 02138, USA

[3]Department of Physics, Harvard University, Cambridge, MA 02138, USA

[4]These authors contributed equally

[5]Lead Contact

*Correspondence: maziz@harvard.edu

https://doi.org/10.1016/j.joule.2018.07.005

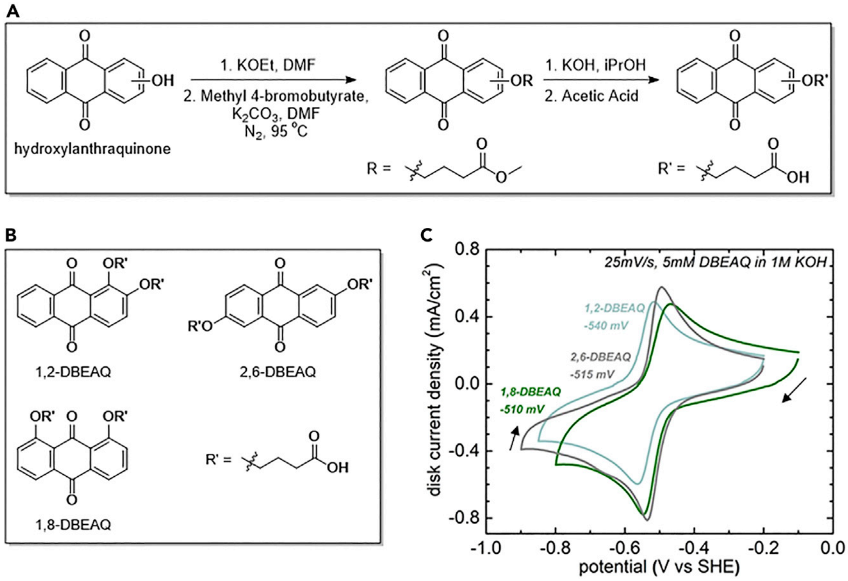

Figure 1. Synthesis and Initial Characterization of DBEAQ

(A) Synthetic approach to functionalize hydroxyanthraquinone with tethered highly alkali-soluble carboxylic groups.

(B) Chemical structures of 1,2-, 2,6-, and 1,8-DBEAQ.

(C) Cyclic voltammograms of 1,2- (blue), 2,6-(gray), and 1,8- (green) DBEAQ. The redox potential vs SHE of each isomer is indicated.

See also Figures S1–S3.

for 2,6-DHAQ under similar conditions, respectively. Several avenues exist for further increasing reactant solubility and the corresponding energy density, such as the use of mixed cations in the electrolytes [15] or mixtures of different DBEAQ isomers or different molecules with nearly the same reduction potential.

All the DBEAQ isomers showed very similar redox potentials between −510 and −540 mV versus standard hydrogen electrode (SHE) (Figure 1C), which would yield battery voltages above 1 V versus ferri-/ferrocyanide posolyte. Despite the increase in reduction potential compared with 2,6-DHAQ (−680 mV versus SHE), their CVs exhibited high reversibility with redox peaks ~40 mV apart, much smaller than the ~90 mV value from 2,6-DHAQ.[4] A Levich analysis was used to obtain the diffusion coefficient of the oxidized form of 2,6-DBEAQ (1.58×10^{-6} cm^2/s; Figure S4), which was then used in a CV simulation of its redox kinetics (Figure S5). The results show, in agreement with an analogous study of the 2,6-DHAQ CV, that the peak shape and separation are consistent with two one-electron reduction steps at different potentials, E_1 and E_2, whose values are modulated by the energetics of semiquinone reduction (see Figure S6 and associated discussion in the Supplemental Information). In comparison with 2,6-DHAQ, which exhibited an E_1-E_2 separation of 60 mV,[4] the 2,6-DBEAQ CV exhibits a much smaller E_1-E_2 separation of 6 mV, implying that 2,6-DHAQ is more thermodynamically susceptible to the formation of semiquinone radicals than 2,6-DBEAQ.

Chemical and Electrochemical Stability Study

We first demonstrate that 2,6-DBEAQ has superior chemical stability over other quinones reported to date, notably including 2,6-DHAQ. As a direct probe of the effect of *O*-alkylation of anthraquinone on its chemical stability, 2,6-DBEAQ was cycled potentiostatically in a volumetrically unbalanced compositionally symmetric cell

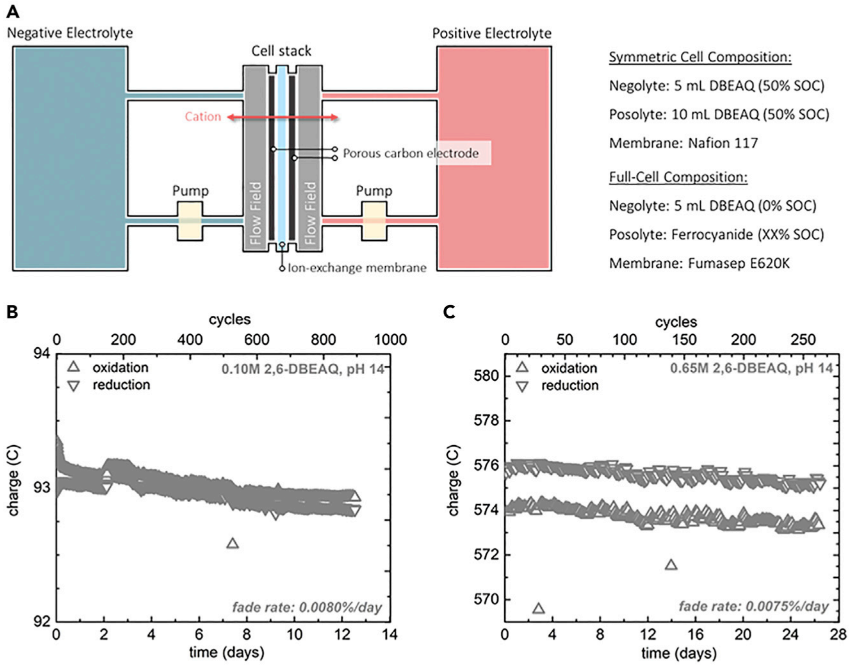

Figure 2. Symmetric Cell Cycling of 2,6-DBEAQ at pH 14

(A) Cell schematic for unbalanced compositionally symmetric cell cycling and full cell cycling.
(B and C) (B) Unbalanced compositionally symmetric cell cycling of 0.10 M 2,6-DBEAQ and (C) 0.65 M 2,6-DBEAQ, showing capacity as a function of time and temporal capacity fade rates from linear fits of the last 5 days of cycling. The capacity-limiting side was 5 mL 2,6-DBEAQ, while the non-capacity-limiting side was 10 mL 2,6-DBEAQ, both at pH 14. Capacities were obtained by full potentiostatic reduction and oxidation at ±0.2 V of the capacity-limiting side; the potential was switched when the magnitude of the current density decayed to 2 mA/cm^2. Note that both y axis scales represent about 2% of the capacity of the capacity-limiting side.
See also Figure S7.

configuration. The symmetric cell configuration, in which the two sides have the same electrolyte composition, is a simple and direct probe of chemical and electrochemical stability of RFB reactants and is described in full in a separate report.[16] Any observed capacity fade is directly related to deactivation of the reactant on the capacity-limiting side in either its oxidized or reduced state because (1) there is negligible reactant crossover with symmetric compositions, (2) changes to membrane resistance do not result in temporal capacity variations in potentiostatic cycling, and (3) the unbalanced volumes permit the capacity-limiting side to be taken to its limiting states of charge (SOCs) despite potential side reactions.

Figure 2 shows a schematic of the cell setup (Figure 2A) and the results of unbalanced compositionally symmetric cell cycling for 2,6-DBEAQ at 0.10 and 0.65 M for durations of 13 and 26 days, respectively (Figures 2B and 2C). In both cases, 2,6-DBEAQ exhibited temporal capacity fade rates of <0.01%/day or <3.0%/year, which suggests a loss mechanism that is first order in 2,6-DBEAQ concentration. In contrast, 2,6-DHAQ cycled in a similar cell configuration demonstrated a much higher temporal fade rate of 5%/day (Figure S7). Temporal capacity fade rates for neutral organic/organometallic RFBs have been summarized elsewhere.[8] Most systems show fade rates in the range of 0.1%–3.5%/day. The temporal fade rate of 2,6-DBEAQ is the lowest ever reported for a quinone-based electrolyte, with the lowest previously reported being for 9,10-anthraquinone-2,6-disulfonate (AQDS) at 0.1%–0.2%/day.[17,18] It is on par with that of a recently reported viologen-based flow battery,[8] which exhibited the highest capacity retention rate for any flow battery in the absence of rebalancing processes, with a temporal capacity fade rate of <0.01%/day in symmetric cell testing.[16]

The origin of the higher chemical stability of 2,6-DBEAQ compared with 2,6-DHAQ is not completely understood; however, we highlight here a few key distinctions that may be responsible. Notably, it is the reduced form of 2,6-DHAQ that has been shown in a previous study to be involved in the loss of redox activity, whereas the reduced form of 2,6-DBEAQ is shown here to be quite stable even at temperatures up to 95°C (see Supplemental Information). Our first observation is that, because the redox potential of 2,6-DBEAQ is ~200 mV higher than that of 2,6-DHAQ, 2,6-DBEAQ should be more stable thermodynamically in its reduced form. Secondly, at high pH, we expect both the reduced hydroquinone core and solubilizing groups to be deprotonated and therefore negatively charged in both molecules. The closer proximity of the negatively charged deprotonated hydroxyl groups in 2,6-DHAQ should lead to larger intramolecular Coulombic repulsion forces, which may contribute to this destabilization of the reduced form of the molecule. Finally, the greater susceptibility to the formation of semiquinone radicals in 2,6-DHAQ, as discussed above, may also be involved in its decreased stability.

The alkyl chain functionalization, while drastically improving lifetime, does not avoid decomposition altogether. By performing elevated temperature chemical stability studies, we have identified that the cleavage of γ-hydroxybutyrate is involved in the decomposition of the oxidized form of 2,6-DBEAQ (Figures S8 and S9), and we have characterized the time course of γ-hydroxybutyrate cleavage at pH 12 and pH 14 and at 0.1 M and 0.5 M concentration (Figures S10 and S11). The results suggest that the half-life of 2,6-DBEAQ at room temperature, pH 14, and 0.1 M concentration in the oxidized form is on the order of 5 years, with substantially slower decomposition in the reduced form relative to the oxidized form and at pH 12 relative to pH 14; these observations are consistent with long RFB lifetime at typical operating cell conditions.

Membrane and Full Cell Studies

Ion-conductive membranes play a critical role in RFB systems in governing the transport of counter ions across the membranes (ionic conductivity) and the simultaneous transport of redox-active species (membrane crossover). In a compositionally asymmetric cell, e.g., 2,6-DBEAQ-ferrocyanide system, capacity fade rate can be greatly exacerbated by the irrecoverable crossover of the reactant to the other side of the electrolyte.[19] To limit capacity fade by this mechanism, while retaining high permselectivity, we surveyed a range of cation-exchange membranes, including the industry standard Nafion-based perfluorosulfonic acid (PFSA) membranes, by characterizing both their K^+ conductivity and permeability of 2,6-DBEAQ and ferricyanide (more permeable than ferrocyanide) (see Experimental Procedures for the customized lab setup). E-600 series membranes, which comprise a non-fluorinated, sulfonated polyaryletherketone-copolymer backbone, delivered the best performance. The membrane displayed a low area specific resistance (ASR) of ~1 $\Omega \cdot cm^2$ in 1 M K^+ solution, which is comparable with Nafion 212. It also showed an extremely low 2,6-DBEAQ and ferricyanide permeability of 5.26×10^{-13} cm^2/s and 4.4×10^{-12} cm^2/s, respectively (Figure S12), which are at least an order of magnitude lower than Nafion 212 systems. To further prove the low permeability of redox-active species, we constructed a low concentration 2,6-DBEAQ-ferri-/ferrocyanide full cell at pH 14, using a Fumasep E-620 (K) membrane. Over a period of galvanostatic cycling testing for 4 days (~880 cycles), the cell showed immeasurably low capacity fade and a current efficiency around ~99.94% (Figure S13). This test is *prima facie* evidence that the low 2,6-DBEAQ permeabilities measured *ex situ* using the nutating table setup translate to negligible crossover of 2,6-DBEAQ in an operating cell and that additional contributions to crossover that are not present in the nutating table tests, such as electromigration and pressure from active pumping of electrolytes,[20] are unimportant. These low permeabilities, together with the fact that Fumasep E-600 series membranes do not contain fluorine, imply that their use in a DBEAQ-ferri-/ferrocyanide full cell affords a potentially robust configuration for a long-lasting RFB with low power cost (in $/kW) for fully installed systems (see A Note on DBEAQ/DHAQ Permeability in Supplemental Information).

To reduce the corrosivity of the system and the ferricyanide decomposition rate, which is exacerbated at high pH,[21,22] we performed the full cell tests of 2,6-DBEAQ at a more moderate electrolyte condition of pH 12. Symmetric cell cycling of 1,2- (Figure S14A) and 1,8-DBEAQ (Figure S14B) at pH 12 showed higher temporal fade rates—greater than 0.1% and 10%/day, respectively—than 2,6-DBEAQ at the same pH (<0.01%/day, Figure S15) and were therefore not tested in full cell experiments. Theoretical calculations suggest that these isomers are more thermodynamically susceptible to hydroxide or water-induced γ-hydroxybutyrate cleavage than 2,6-DBEAQ (see Table S4). Given the 0.6 M solubility measured for 2,6-DBEAQ at pH 12 (Table S2), subsequent cell tests were performed at 0.5 M in order to examine the performance of a full cell with reasonable energy density. From the Pourbaix diagram of 2,6-DBEAQ (Figure S16A), its reduction potential becomes pH independent above pH 11.5 and is not expected to change during cell cycling. Polarization and capacity utilization measurements with a negolyte containing 0.5 M 2,6-DBEAQ are shown in Figure 3. Polarization studies (Figure 3A) at room temperature showed a near-linear relationship between current density and voltage at currents close to the open-circuit voltage (OCV), which increased from 0.97 V at 10% SOC to 1.12 V at 100% SOC (Figure 3B). Between 80% and 90% of the polarization ASR is accounted for by the high-frequency resistance measured using electrochemical impedance spectroscopy (EIS), which largely reflects membrane resistance. A peak galvanic power density of 0.24 W/cm^2 was realized at 100% SOC (Figure S17). This power density is about half of that previously reported in a 2,6-DHAQ-ferrocyanide cell,[4] owing to the higher OCV of the latter (1.20 V as opposed to 1.05 V at 50% SOC) and smaller ASR (0.858 Ω cm^2 as opposed to 1.2 Ω cm^2 at 50% SOC). When voltage and current have a linear, ohmic relationship, the peak galvanic power density is given by $p_{max} = V_{OC}^2/r$, where V_{OC} is the open-circuit potential and r is the ASR. The low permeability of the Fumasep membrane to the fastest-crossing species (i.e., 200 years required for 50% loss through crossover of ferricyanide) permits, in principle, a 4-fold reduction in the membrane thickness, which would raise the power density significantly.

In order to avoid temporal variations in accessible capacity during full cell cycling caused by changes in membrane resistance,[16] each galvanostatic half cycle was finished with a potential hold at the potential limit (1.4 V after charge, 0.6 V after discharge) until the magnitude of the current density fell below 2 mA/cm^2. Over a 5-day test period, a capacity fade rate of 0.05%/day or 0.001%/cycle was observed (Figure 4A). A parallel cycling test was performed in which a potentiostatic charge-discharge cycle was executed after every 20 galvanostatic cycles; a capacity fade rate of 0.04%/day was observed in that case (Figure 4B). It has been shown that capacity retention rates using both cycling protocols yield virtually identical results.[16]

These full cell measurements, however, showed roughly 4-fold increase in capacity fade compared with the <0.01%/day observed during symmetric cycling tests

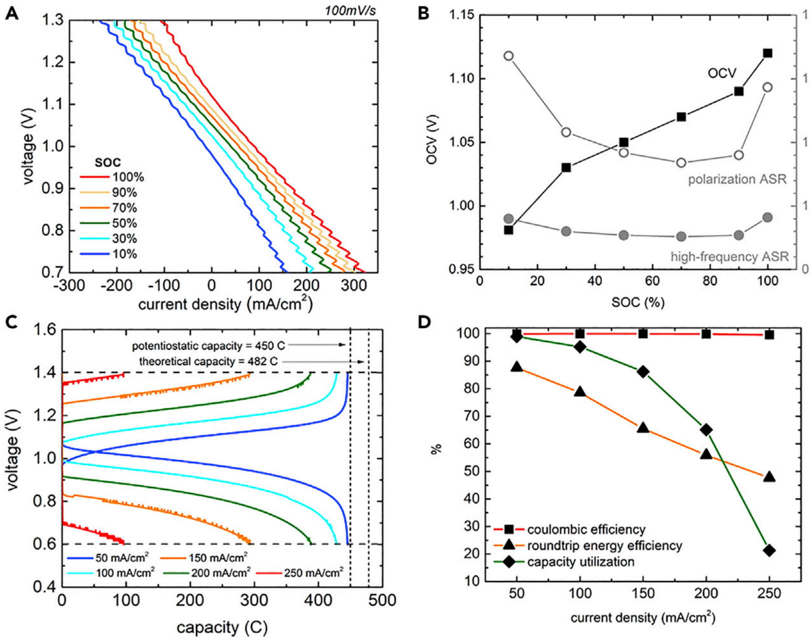

Figure 3. Polarization Measurements of 2,6-DBEAQ Full Cell at pH 12

(A) Cell voltage versus discharge current density at room temperature at 10%, 30%, 50%, 70%, 90%, and 100% SOC. Electrolytes comprised 5 mL of 0.5 M 2,6-DBEAQ (negolyte) at pH 12 (10 mM KOH) and 38 mL of 0.3 M potassium ferrocyanide and 0.1 M potassium ferricyanide (posolyte) at pH 12.

(B) OCV, high-frequency, and polarization ASR versus SOC.

(C) Galvanostatic charge and discharge curves from 25 to 250 mA/cm^2. The vertical dashed lines indicate the maximum capacity realized with potentiostatic charge and discharge at the voltage cutoffs (1.4 and 0.6 V, respectively), as well as the theoretical capacity.

(D) Coulombic efficiency, round-trip energy efficiency, and capacity utilization as a percentage of potentiostatic capacity versus current density.

(Figures 2B and 2C), suggesting additional capacity fade mechanisms not observed during symmetric cell studies. In-depth chemical and electrochemical analysis (Figure S18) was performed to probe the chemical decomposition and crossover of DBEAQ from the capacity-limiting side. Electrolytes in a cell compositionally identical to that in Figure 4A but cycled for 11 days were subjected to nuclear magnetic resonance (NMR) (Figure S18A) and CV (Figure S18B) analysis. From these results, no evidence of DBEAQ decomposition and crossover was found after examining the negolyte and posolyte before and after cycling. Based on the detection limit of NMR (0.1 mM DBEAQ) and CV techniques under the experimental conditions chosen, the upper limit of the capacity fade rate caused by 2,6-DBEAQ decomposition and/or membrane crossover was ~0.01%/day, similar to our symmetric cell study. We therefore hypothesize that other capacity fade mechanisms, such as precipitation of 2,6-DBEAQ in the posolyte after crossing over, might be operative but untraceable by NMR and CV techniques due to the slow capacity fade rate, which corresponds to a total loss of <0.5% of 2,6-DBEAQ over a 6-day testing period. One other such mechanism might be leakage of the negolyte due to poorer adhesion between the thinner Fumasep membrane and the Viton gasket in the full cell than between Nafion N117 and the gasket in the symmetric cell. Indeed, the total capacity fade in Figure 4B corresponds to a total loss over the entire 6-day cycling period of ~10 μL of negolyte volume, which is roughly one-fifth of a droplet. When translated to an equivalent current density (0.5 μA/cm^2), this negolyte loss rate is well within expectation for seepage of the electrolyte into spaces between

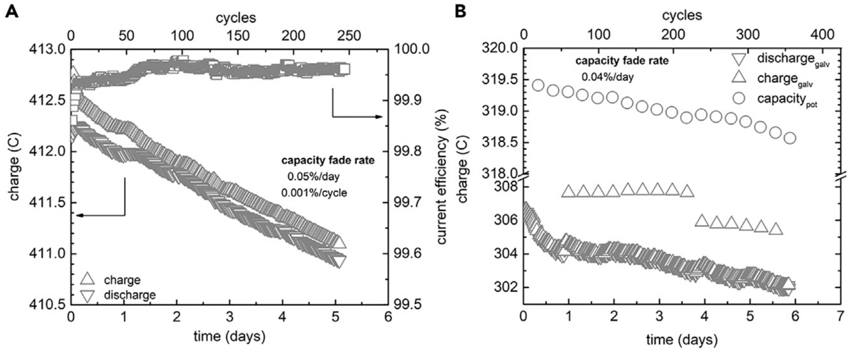

Figure 4. Extended Full Cell Cycling of 2,6-DBEAQ at 0.5 M and pH 12

(A) Current efficiency (squares) and charge (upward-pointing triangles) and discharge (downward-pointing triangles) capacity versus time and cycle number for a negolyte-limited 2,6-DBEAQ-$Fe(CN)_6$ cell. The cell was cycled galvanostatically at 100 mA/cm^2 between 1.4 and 0.6 V, and each half cycle ended with a potentiostatic hold until the magnitude of the current density fell below 2 mA/cm^2. The negolyte comprised 5 mL of 0.5 M 2,6-DBEAQ at pH 12 while the posolyte comprised 30 mL of 0.3 M potassium ferrocyanide and 0.1 M potassium ferricyanide at pH 12.
(B) Evolution of charge (upward-pointing triangles) and discharge (downward-pointing triangles) capacity for extended cell cycling at 100 mA/cm^2. After every 20th galvanostatic cycle, a potentiostatic charge-discharge cycle was performed, the discharge capacity of which is shown (open circles). Because the concentration of oxidized 2,6-DBEAQ is at its maximum after each potentiostatic discharge, the capacity of the galvanostatic charge step immediately following potentiostatic charge-discharge is higher than in subsequent cycles. This particular cell showed only ~65% of its theoretical capacity because a large fraction of salt was left over from the synthesis of 2,6-DBEAQ.

the gaskets and/or interface between the membrane and gaskets, compared with an analogous leak rate estimated from a previous study of capacity fade in an anthraquinone-based flow battery with this cell architecture (0.09–0.12 mA/cm^2).[19]

Quinones for aqueous flow batteries have been the subject of intensive research since their recent debut in this application. This work demonstrates that the simple functionalization with bulky charged groups can greatly extend the calendar life and cycle life; raise the solubility, leading to a theoretical energy density of 17 Wh/L with possible routes to further increases; operate with fluoropolymer-free membranes at pH as low as 12 while maintaining the voltage against $Fe(CN)_6^{3-/4-}$ above 1 V; and perform with peak power density of 0.24 W/cm^2 at room temperature with possible routes to further increases. These properties appear to meet all of the technical requirements commonly understood to be necessary for aqueous RFB commercialization.

At the large production volumes necessary for gigawatt-scale grid storage, it is possible that DBEAQ may approach the cost of other functionalized anthraquinones, such as DHAQ and AQDS, the latter of which was recently estimated to be between \$0.92/kg and \$3.92/kg.[23] Using \$2.40/kg as a mid-range cost, this results in a capital cost of \$17.60/kWh for the 2-electron-accepting DBEAQ in the negolyte in a 1.05 V battery. Similarly, we estimate the industrial-scale cost of potassium ferrocyanide to be around \$2.15/kg,[24] which amounts to a capital cost of about \$32/kWh for the posolyte (see Estimated Cost of Electrolytes in the Supplemental Information). At \$50/kWh, the total capital cost of these electrolytes stands at less than one-third of the cost of an all-vanadium electrolyte, for which the vanadium alone is currently priced at \$160/kWh. Using a fluorine-free membrane such as Fumasep E−620 (K) should result in a product of membrane cost (<\$25/m^2 at large production volumes) and ASR (<1.5 Ω cm^2) that is below \$5/mΩ, which adds negligible cost to the system.[25] Thus, if the DBEAQ production cost at scale turns out to be nearly as low as for AQDS and DHAQ,[23,26] then this chemistry may have serious commercial potential, and DBEAQ-based flow batteries may be instrumental in accelerating the penetration of wind and photovoltaic electricity.

EXPERIMENTAL PROCEDURES

Synthesis and Chemical Characterization

Synthesis of 4,4′-((9,10-Anthraquinone-2,6-diyl)dioxy)dibutyric Acid

2,6-DHAQ was purchased from AK Scientific. Methyl 4-bromobutyrate was purchased from VWR. All other chemicals were purchased from Sigma-Aldrich. All chemicals were used as received unless specified otherwise.

Dimethyl 4,4′-((9,10-anthraquinone-2,6-diyl)dioxy)dibutyrate (1). 2,6-DHAQ was first converted to its dipotassium salt (2,6-$DHAQK_2$) by adding 2,6-DHAQ (5 g, 20.8 mmol) to a 250 mL oven-dried flask of dimethylformamide (250 mL). Under vigorous stirring, potassium ethoxide (6.1 g, 72.9 mmol) was added. The mixture solution was stirred at room temperature for 15 min. For the *O*-alkylation reaction, 2,6-$DHAQK_2$ (6.5 g, 20.8 mmol) was mixed with anhydrous K_2CO_3 (14.3 g, 104 mmol) and methyl 4-bromobutyrate (12.4 mL, 104 mmol). The reaction mixture was then heated to 95°C overnight. After cooling to 0°C, deionized (DI) water (150 mL) was added to the mixture to dissolve inorganic salt and to precipitate the ester precursor of DBEAQ. The precipitate was vacuum filtered and washed thoroughly with DI water (50 mL). The product was analyzed by ^1H NMR and used for the next step reaction without further purification. Final yield, 87%.

4,4′-((9,10-Anthraquinone-2,6-diyl)dioxy)dibutyric Acid (2). The ester precursor of DBEAQ (1 g, 2.23 mmol) was added along with KOH (0.52 g, 9 mmol) to a flask filled with a water-isopropanol mixture (2:1 v/v, 60 mL). The solution was stirred vigorously and heated to 60°C for 12 hr. During the reaction, all solids dissolved, and the solution became a dark red color. After the reaction, the solution was transferred to a larger 500 mL flask and diluted with DI water (200 mL). Glacial acetic acid was added until the pH of the solution dropped to 4. The mixture was stirred vigorously for 1 hr, followed by vacuum filtration and thorough washing with DI water (100 mL). The product was vacuum dried, analyzed by ^1H NMR, and used for electrochemical measurement without further purification. Final yield, 99%.

The ^1H NMR spectrum of 4,4′-((9,10-anthraquinone-2,6-diyl)dioxy)dibutyric acid is shown in Figure S1. 1,8- and 1,2-isomers were synthesized similarly, using 1,2-DHAQ and 1,8-DHAQ as precursors. Potassium tert-butoxide (8.16 g, 72.9 mmol) replaced potassium ethoxide to deprotonate the 1,2-DHAQ and 1,8-DHAQ isomers because of the higher pK_a of the hydroxyl groups of these isomers. ^1H NMR spectra of the final products are shown in Figures S2 and S3, respectively.

Electrochemical Characterization

Cyclic Voltammetry and Rotating Disk Electrode Measurements

Glassy carbon was used as the working electrode for all three-electrode CV tests. Rotating disk electrode experiments were conducted using a Pine Instruments Modulated Speed Rotator AFMSRCE equipped with a 5 mm diameter glassy carbon working electrode, a Ag/AgCl reference electrode (BASi, pre-soaked in 3 M NaCl solution), and a graphite counter electrode. The electrode was rotated at a specific speed while the voltage was swept linearly from −0.4 to −0.11 V versus Ag/AgCl (Figure S4A). The diffusion coefficient of the oxidized form of 2,6-DBEAQ was calculated using the Levich equation, which relates the mass-transport-limited current to the number of electrons transferred (n), the area of the electrode (A), and the concentration of redox-active species in the electrolyte (C), by plotting the mass-transport-limited current against the square root of the rotation rate (Figure S4B) with the following parameters: $n = 2$, $F = 96{,}485$ C/mol, $A = 0.196\ \mathrm{cm}^2$, $C = 5$ mM, kinematic viscosity of 1 M KOH $\nu = 1.08 \times 10^{-6}\ \mathrm{m}^2/\mathrm{s}$. The resulting value of the diffusion coefficient for the oxidized form of 2,6-DBEAQ is $1.58 \times 10^{-6}\ \mathrm{cm}^2/\mathrm{s}$.

Symmetric and Full Cell Measurements

Flow battery experiments were constructed with cell hardware from Fuel Cell Tech (Albuquerque, NM) assembled into a zero-gap flow cell configuration, similar to a previous report.[4] Pyrosealed POCO graphite flow plates with serpentine flow patterns were used for both electrodes. Each electrode comprised a 5 cm^2 geometric surface area covered by a stack of three or four sheets of Sigracet SGL 39AA porous carbon paper pre-baked in air overnight at 400°C.

For symmetric cell tests, a sheet of Nafion 117 membrane soaked overnight in 1 M KOH served as the ion-selective membrane between the carbon electrodes, whereas for full cell tests, a Fumasep E−620 (K) membrane was used. The outer portion of the space between the electrodes was gasketed by Viton sheets with the area over the electrodes cut out. Torque applied during cell assembly was 60 lb-in (6.78 Nm) on each of 8 bolts. The electrolytes were fed into the cell through fluorinated ethylene propylene tubing at a rate of 60 mL/min, controlled by Cole-Parmer Masterflex L/S peristaltic pumps. All cells were run inside a nitrogen-filled glove box with an O_2 partial pressure of about 1–2 ppm. Cell polarization measurements, impedance spectroscopy, and charge-discharge cycling were performed using a Biologic VSP 300 potentiostat.

Potentiostatic symmetric cell cycling was performed according to a reported procedure[16] in order to assess the temporal chemical stability of DBEAQ, independently of any variations in apparent capacity as a result of changes to membrane resistance, and in a configuration where there is negligible water or reactant crossover due to the same DBEAQ concentration being used in both electrolytes. 7.5 mL of 2,6-DBEAQ was fully reduced (i.e., charged to 100% SOC) against a posolyte of excess potassium ferrocyanide and then mixed with 7.5 mL of oxidized 2,6-DBEAQ (0% SOC) to afford a 2,6-DBEAQ electrolyte at 50% SOC. 5 mL of the resulting electrolyte was used as the capacity-limiting side of a volumetrically unbalanced compositionally symmetric cell, while the remaining 10 mL was used as the non-capacity-limiting side, i.e., with twice the nominal capacity of the capacity-limiting side. The capacity-limiting side was then cycled potentiostatically between 0% and ~100% SOC with potential limits of ± 0.2 V versus the non-capacity-limiting side, switched when the absolute value of the current density decayed to 2 $\mathrm{mA/cm}^2$, which is ~3× higher than the background current.

Full cell cycling (i.e., with a ferro-/ferricyanide-based posolyte) was performed with the same flow cell hardware but with a Fumasep E−620 (K) membrane due to its high conductivity and low permeability of DBEAQ and ferricyanide compared with other membranes (see Supplemental Information). For studies at pH 14, the posolyte volume was 30 mL, and its composition, when assembled, was 0.20 M potassium ferrocyanide, 0.08 M potassium ferricyanide, and 1 M KOH. The negolyte was prepared by dissolving 0.1 M 2,6-DBEAQ in its oxidized form in 1.2 M KOH solution, resulting in 0.1 M 2,6-DBEAQ, 1.2 M K^+, and 1 M OH^- electrolyte solution. For studies at pH 12, both electrolytes comprised 10 mM OH^-; the pH was checked both with a pH meter and pH paper and adjusted where necessary. For all full cell studies, the negolyte was assembled in the fully discharged state.

Galvanostatic cycling was performed at ±0.1 A/cm^2 at room temperature with voltage limits of 0.6 and 1.4 V. To obtain the polarization curves, the cell was first charged to the desired state of charge and then polarized via linear sweep voltammetry at a rate of 100 mV/s. This method was found to yield polarization curves very close to point-by-point galvanostatic holds, yet to impose minimal perturbation to the SOC of the small-electrolyte-volume cell. EIS was performed at SOCs between 10% and 100% at open-circuit potential with a 10 mV perturbation and with frequency ranging from 1 to 300,000 Hz.

Permeability Measurements

The permeability of the oxidized form of 2,6-DBEAQ and potassium ferricyanide across a Fumasep E-620 (K) membrane was evaluated with a lab-made two-compartment cell. In the first case, the donating side was filled with a solution of 2,6-DBEAQ (0.1 M) in 1.6 M KOH, while the receiving side was filled with 1.6 M KOH. For potassium ferricyanide permeability, the donating side was filled with potassium ferricyanide (0.3 M) in 1 M KOH, while the receiving side was filled with 1.9 M KOH. Both compartments had the same volume. The cell was continuously agitated on a nutating table. At different time intervals, aliquots were taken from the receiving side, diluted, characterized by UV-visible spectrophotometry, and replaced by fresh KOH solution. The electrolyte volumes on both sides were checked periodically to ensure that there was negligible water flux across the membrane, which might affect the apparent reactant permeability. The concentration was calculated from a calibration curve and the permeability of 2,6-DBEAQ was calculated based on Fick's law using the following equation:

$$P = \frac{\Delta \ln\left(1 - \frac{2c_t}{c_0}\right)\left(\frac{V_o l}{2A}\right)}{\Delta t},$$

where P is permeability (cm^2/s), A is the effective membrane area (cm^2), t is elapsed time (s), c_t (mol/L) is the concentration of active species in the receiving side at time t, V_o is the volume of the solution in either compartment (5 cm^3), l is the thickness of the membrane (~20 μm), c_o is the concentration of 2,6-DBEAQ in the donating side at time zero (0.1 mol/L), and Δ represents a finite difference.

Solubility Tests

Solubility limits of all DBEAQ isomers were measured in their oxidized forms by adding the potassium salt of DBEAQ (prepared by reacting DBEAQ with potassium hydroxide in water) until no further solid could be dissolved. After filtering the mixture through a polytetrafluoroethylene 0.45 μm syringe filter, a saturated solution of DBEAQ in KOH was obtained. The saturated solution was then diluted by a known amount, and the concentration was evaluated by UV-visible spectrometry (Ocean Optics Flame-S Spectrometer Assembly) at 280 and 364 nm. The concentration was calculated according to a pre-calibrated absorbance-concentration curve of known concentrations of DBEAQ. Solubility of the oxygen-sensitive reduced form of DBEAQ was not measured but was assumed to be higher than the oxidized form because (1) no precipitation after full electrochemical reduction of DBEAQ was observed and (2) increasing the number of negative charges from two for DBEAQ in the oxidized form to four for DBEAQ in the reduced form is expected to make quinone-quinone interactions even more unfavorable and increase its solubility.[27]

SUPPLEMENTAL INFORMATION

Supplemental Information includes Supplemental Experimental Procedures, 18 figures, 2 schemes, and 4 tables and can be found with this article online at https://doi.org/10.1016/j.joule.2018.07.005.

ACKNOWLEDGMENTS

This research was supported initially by U.S. DOE ARPA-E award DE-AR-0000348 and subsequently by U.S. DOE award DE-AC05-76RL01830 through PNNL subcontract 304500, by Innovation Fund Denmark via the Grand Solutions project "ORBATS" file no. 7046-00018B, by the Massachusetts Clean Energy Technology Center, and by the Harvard School of Engineering and Applied Sciences. D.A.P. acknowledges funding support from the NSF Graduate Research Fellowship Program. We thank Nada Aissami for help with permeability measurements.

AUTHOR CONTRIBUTIONS

K.L. designed the molecule. Y.J. designed the synthetic route and synthesized the molecule; subsequent syntheses were performed by K.L. and E.F.K. K.L., Y.J., and E.F.K. performed molecular characterization. M.-A.G. and D.G.K. performed symmetric cell tests. D.G.K. performed full cell tests. D.D.P. performed permeability tests and membrane selection and assisted with cell assembly. E.F.K. performed chemical analysis of cycled electrolytes. D.A.P. performed chemical analysis and stability studies. D.P.T. performed theoretical calculations under the supervision of A.A.-G. R.G.G. supervised the molecular synthesis and characterization. M.J.A. supervised the cell assembly, electrolyte composition selection, and performance evaluation. D.G.K. and M.J.A. drafted the manuscript. All authors edited the manuscript.

DECLARATION OF INTERESTS

Harvard University has filed a patent application on the materials described in this paper.

Received: March 16, 2018
Revised: May 8, 2018
Accepted: July 3, 2018
Published: July 23, 2018

REFERENCES

1. Soloveichik, G.L. (2015). Flow batteries: current status and trends. Chem. Rev. *115*, 11533.
2. Huskinson, B., Marshak, M.P., Suh, C., Er, S., Gerhardt, M.R., Galvin, C.J., Chen, X., Aspuru-Guzik, A., Gordon, R.G., and Aziz, M.J. (2014). A metal-free organic-inorganic aqueous flow battery. Nature *505*, 195.
3. Janoschka, T., Martin, N., Martin, U., Friebe, C., Morgenstern, S., Hiller, H., Hager, M.D., and Schubert, U.S. (2015). An aqueous, polymer-based redox-flow battery using non-corrosive, safe, and low-cost materials. Nature *527*, 78.
4. Lin, K., Chen, Q., Gerhardt, M.R., Tong, L., Kim, S.B., Eisenach, L., Valle, A.W., Hardee, D., Gordon, R.G., Aziz, M.J., and Marshak, M.P. (2015). Alkaline quinone flow battery. Science *349*, 1529.
5. Lin, K., Gómez-Bombarelli, R., Beh, E.S., Tong, L., Chen, Q., Valle, A., Aspuru-Guzik, A., Aziz, M.J., and Gordon, R.G. (2016). A redox-flow battery with an alloxazine-based organic electrolyte. Nat. Energy *1*, 16102.
6. Hoober-Burkhardt, L., Krishnamoorthy, S., Yang, B., Murali, A., Nirmalchandar, A., Surya Prakash, G.K., and Narayanan, S.R. (2017). A new Michael-reaction-resistant benzoquinone for aqueous organic redox flow batteries. J. Electrochem. Soc. *164*, A600.
7. Yang, B., Hoober-Burkhardt, L., Krishnamoorthy, S., Murali, A., Prakash, G.K.S., and Narayanan, S.R. (2016). High-performance aqueous organic flow battery with quinone-based redox couples at both electrodes. J. Electrochem. Soc. *163*, A1442.
8. Beh, E.S., De Porcellinis, D., Gracia, R.L., Xia, K.T., Gordon, R.G., and Aziz, M.J. (2017). A neutral pH aqueous organic–organometallic redox flow battery with extremely high capacity retention. ACS Energy Lett. *2*, 639.
9. DeBruler, C., Hu, B., Moss, J., Liu, X., Luo, J., Sun, Y., and Liu, T.L. (2017). Designer two-electron storage viologen anolyte materials for neutral aqueous organic redox flow batteries. Chem *3*, 1.
10. Janoschka, T., Morgenstern, S., Hiller, H., Friebe, C., Wolkersdorfer, K., Hauptler, B., Hager, M.D., and Schubert, U.S. (2015). Synthesis and characterization of tempo- and viologen-polymers for water-based redox-flow batteries. Polym. Chem. *6*, 7801.
11. Liu, T., Wei, X., Nie, Z., Sprenkle, V., and Wang, W. (2015). A total organic aqueous redox flow battery employing a low cost and sustainable methyl viologen anolyte and 4-Ho-tempo catholyte. Adv. Energy Mater. *6*, 1501449.

12. Wei, X., Xu, W., Vijayakumar, M., Cosimbescu, L., Liu, T., Sprenkle, V., and Wang, W. (2014). Tempo-based catholyte for high-energy density nonaqueous redox flow batteries. Adv. Mater. *26*, 7649.

13. Winsberg, J., Muench, S., Hagemann, T., Morgenstern, S., Janoschka, T., Billing, M., Schacher, F.H., Hauffman, G., Gohy, J.-F., Hoeppener, S., et al. (2016). Polymer/zinc hybrid-flow battery using block copolymer micelles featuring a tempo corona as catholyte. Polym. Chem. *7*, 1711.

14. Winsberg, J., Stolze, C., Muench, S., Liedl, F., Hager, M.D., and Schubert, U.S. (2016). Tempo/phenazine combi-molecule: a redox-active material for symmetric aqueous redox-flow batteries. ACS Energy Lett. *1*, 976.

15. Esswein, A.J., Goeltz, J., and Amadeo, D. (2014). High solubility iron hexacyanides, US patent 2014/0051003 A1 (2/20/2014 2014), filed May 6, 2013, and granted Mar 27, 2018.

16. Goulet, M.-A., and Aziz, M.J. (2018). Flow battery molecular reactant stability determined by symmetric cell cycling methods. J. Electrochem. Soc. *165*, 7, A1466.

17. Khataee, A., Wedege, K., Drazevic, E., and Bentien, A. (2017). Differential pH as a method for increasing cell potential in organic aqueous flow batteries. J. Mater. Chem. A. *5*, 21875–21882.

18. Gerhardt, M.R., Tong, L., Gómez-Bombarelli, R., Chen, Q., Marshak, M.P., Galvin, C.J., Aspuru-Guzik, A., Gordon, R.G., and Aziz, M.J. (2017). Anthraquinone derivatives in aqueous flow batteries. Adv. Energy Mater. *7*, 1601488.

19. Chen, R., and Hempelmann, R. (2016). Ionic liquid-mediated aqueous redox flow batteries for high voltage applications. Electrochem. Commun. *70*, 56.

20. Darling, R., Gallagher, K., Xie, W., Su, L., and Brushett, F. (2015). Transport property requirements for flow battery separators. J. Electrochem. Soc. *163*, A5029.

21. Luo, J., Sam, A., Hu, C., DeBruler, Wei, X., Wang, W., and Liu, T.L. (2017). Unraveling pH dependent cycling stability of ferricyanide/ferrocyanide in redox flow batteries. Nano Energy *42*, 215–221.

22. Reece, S.Y. (2016). Metal complexes of substituted catecholates and redox flow batteries containing the same, US patent US20160149251A1, filed November 25, 2015.

23. Dieterich, V., Milshtein, J., Barton, J., Carney, T., Darling, R., and Brushett, F. (2018). Estimating the cost of organic battery active materials: a case study on anthraquinone disulfonic acid. Transl. Mater. Res. https://doi.org/10.1088/2053-1613/aacb0e.

24. Yuan, Z., Duan, Y., Liu, T., Zhang, H., and Li, X. (2018). Toward a low cost alkaline zinc-iron flow battery with a polybenzimidazole custom membrane for stationary energy storage. iScience. https://doi.org/10.1016/j.isci.2018.04.006.

25. Darling, R.M., Gallagher, K.G., Kowalski, J.A., Ha, S., and Brushett, F.R. (2014). Pathways to low-cost electrochemical energy storage: a comparison of aqueous and nonaqueous flow batteries. Energy Environ. Sci. *7*, 3459.

26. Yang, Z., Tong, L., Tabor, D.P., Beh, E.S., Goulet, M.-A., De Porcellinis, D., Aspuru-Guzik, A., Gordon, R.G., and Aziz, M.J. (2017). Alkaline benzoquinone aqueous flow battery for large-scale storage of electrical energy. Adv. Energy Mater. *7*, 1702056.

27. Karandur, D., Wong, K.Y., and Pettitt, B.M. (2014). Solubility and aggregation of Gly(5) in water. J. Phys. Chem. B *118*, 9565.

JOUL, Volume *2*

Supplemental Information

Alkaline Quinone Flow Battery

with Long Lifetime at pH 12

David G. Kwabi, Kaixiang Lin, Yunlong Ji, Emily F. Kerr, Marc-Antoni Goulet, Diana De Porcellinis, Daniel P. Tabor, Daniel A. Pollack, Alán Aspuru-Guzik, Roy G. Gordon, and Michael J. Aziz

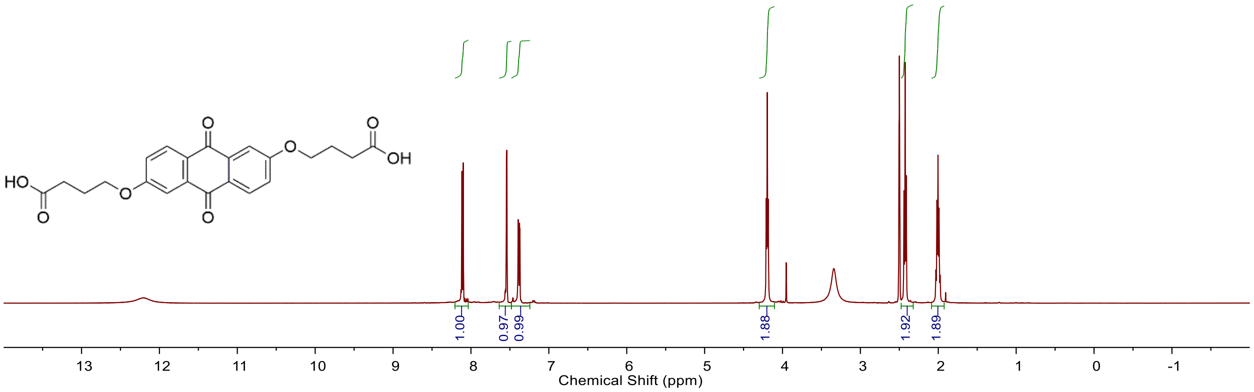

Figure S1. ^{1}H NMR spectrum of 2,6-DBEAQ. ^{1}H NMR (500 MHz, DMSO-d_6): δ 11.79 (s, 2H), 8.11 (d, *J* = 8.6 Hz, 2H), 7.54 (d, *J* = 2.6 Hz, 2H), 7.38 (dd, *J* = 8.7, 2.6 Hz, 2H), 4.20 (t, *J* = 6.4 Hz, 4H), 2.43 (t, *J* = 7.3 Hz, 4H), 2.00 (m, 4H). Solvent peaks are those that are not integrated. Final yield: 87%.

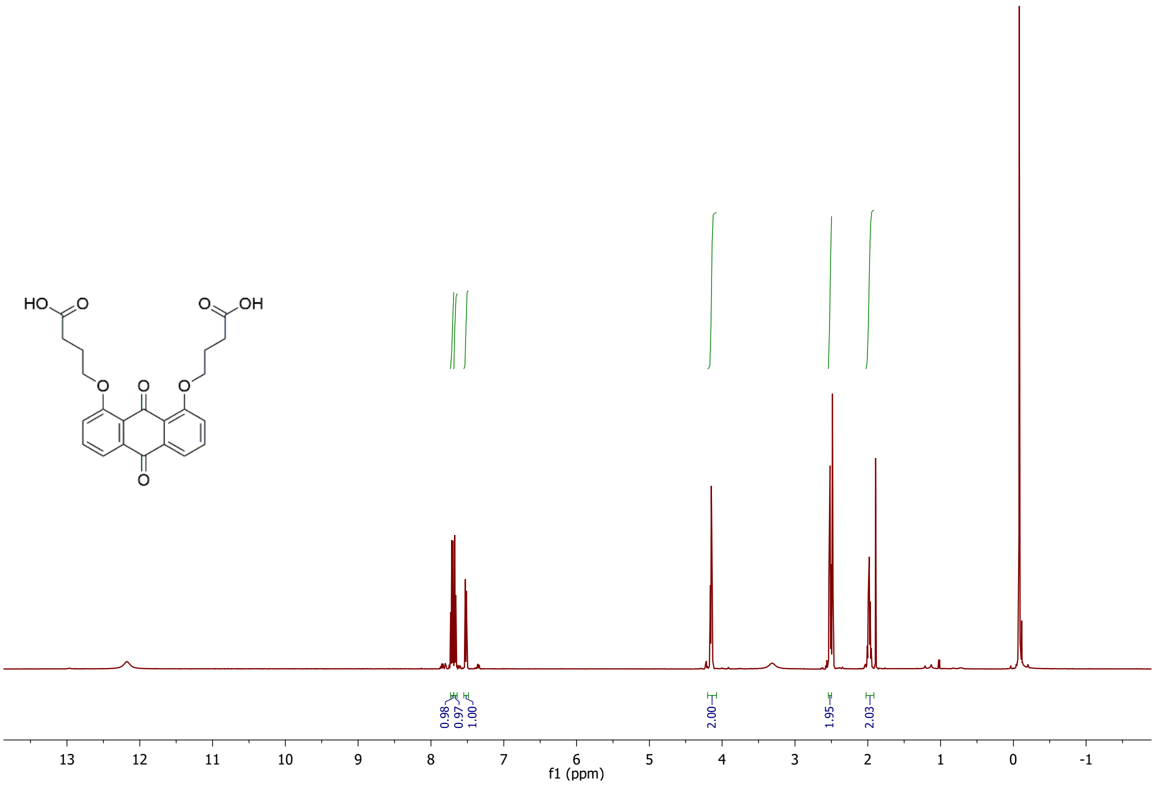

Figure S2. ^{1}H NMR spectrum of 1,8-DBEAQ. ^{1}H NMR (500 MHz, DMSO-d_6): δ 12.17 (s, 2H), 7.71 (m, 2H), 7.65 (m, 2H), 7.52 (dd, *J* = 8.3, 1.3 Hz, 2H), 4.15 (t, *J* = 6.3 Hz, 4H), 2.53 (t, *J* = 7.3 Hz, 4H), 1.89 (m, 4H). Final yield: 64.4%.

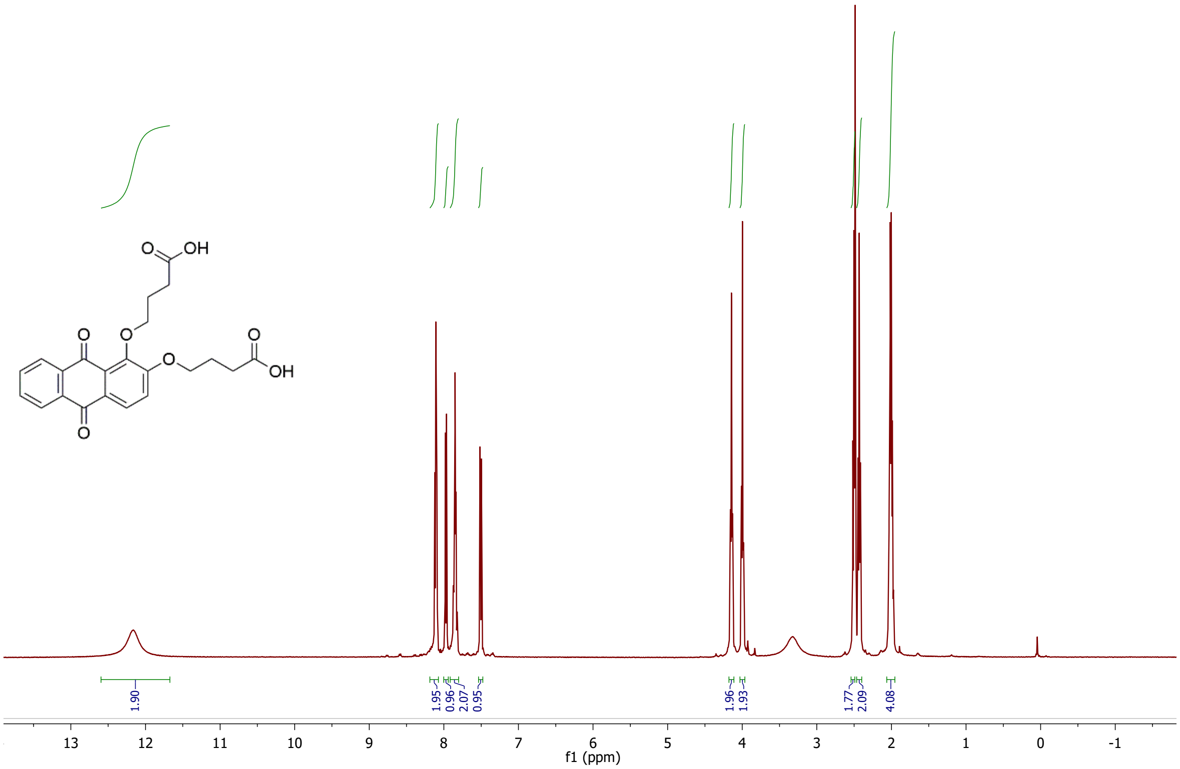

Figure S3. ^{1}H NMR spectrum of 1,2-DBEAQ. ^{1}H NMR (500 MHz, DMSO-d_6): δ 12.15 (s, 2H), 8.11 (m, 2H), 7.97 (dd, *J* = 8.6, 1.4 Hz, 1H), 7.85 (m, 2H), 7.51 (d, *J* = 8.7 Hz, 1H), 4.14 (t, *J* = 6.4 Hz, 2H), 4.00 (t, *J* = 6.2 Hz, 2H), 2.51 (t, *J* = 7.4 Hz, 2H), 2.43 (t, *J* = 7.2 Hz, 2H), 2.01 (m, 4H). Final yield: 72.1%.

Compound	**Conditions**	**Maximum Solubility (M)**
Potassium Ferrocyanide	KOH, pH 14	0.5
	KOH, pH 12	1.2 – 1.3
Potassium Ferricyanide	KOH, pH 14	1.05 –1.13
	KOH, pH 12	1.8 – 2.0
2,6-DBEAQ	KOH, pH 14	1.10
	KOH, pH 12	0.60

Table S1. Effect of pH and counter-ion on maximum solubilities of potassium ferrocyanide, potassium ferricyanide, and 2,6-DBEAQ in KOH. Ranges represent uncertainties in solubility based on different peaks used in UV-Vis calibration measurements.

Negolyte	**Solubility (M) at pH 14 (pH 12)**	**Cell Voltage (V)**	**Theoretical Energy Density (Wh/L) at pH 14 (pH 12)**
2,6-DHAQ	0.6	1.20	11.4
2,6-DBEAQ	1.1 (0.60)	1.05	11.5 (17.2)
1,2-DBEAQ	0.9	1.04	10.9
1,8-DBEAQ	0.75	1.01	10.2

Table S2. Effect of solubility and full cell voltage when paired against a potassium ferrocyanide-based posolyte on theoretical energy densities of 2,6-DHAQ and different DBEAQ isomers, with the solubility of potassium ferrocyanide estimated to be 0.5 M at pH 14 and 1.25 M at pH 12. Solubilities for potassium ferricyanide and 2,6-DBEAQ at pH 14 and 12 are reported in Table S1. For 2,6-DBEAQ and 2,6-DHAQ, cell voltages were obtained from the OCV at 50% SOC from full cell tests, whereas differences in CV-obtained redox potentials between DBEAQ and potassium ferri/ferrocyanide were used for 1,2- and 1,8-DBEAQ.

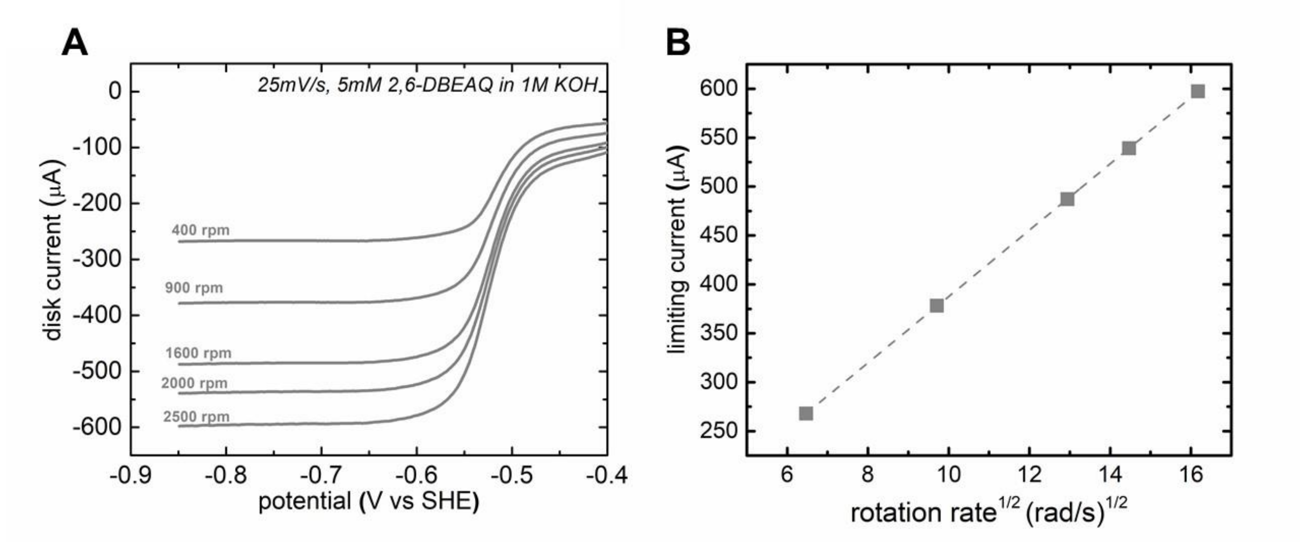

Figure S4. (a) Rotating Disk Electrode study of the reduction of 5 mM 2,6-DBEAQ in 1M KOH on a glassy carbon electrode at rotation rates between 400 and 2500 rpm. (b) Levich plot (limiting current *vs* square root of rotation rate in rad/s) of 5 mM 2,6-DBEAQ in 1 M KOH. Data are taken from the current at -0.8 V *vs* SHE. The slope yields a diffusion coefficient for the oxidized form of 2,6-DBEAQ of 1.58×10^{-6} cm^2/s.

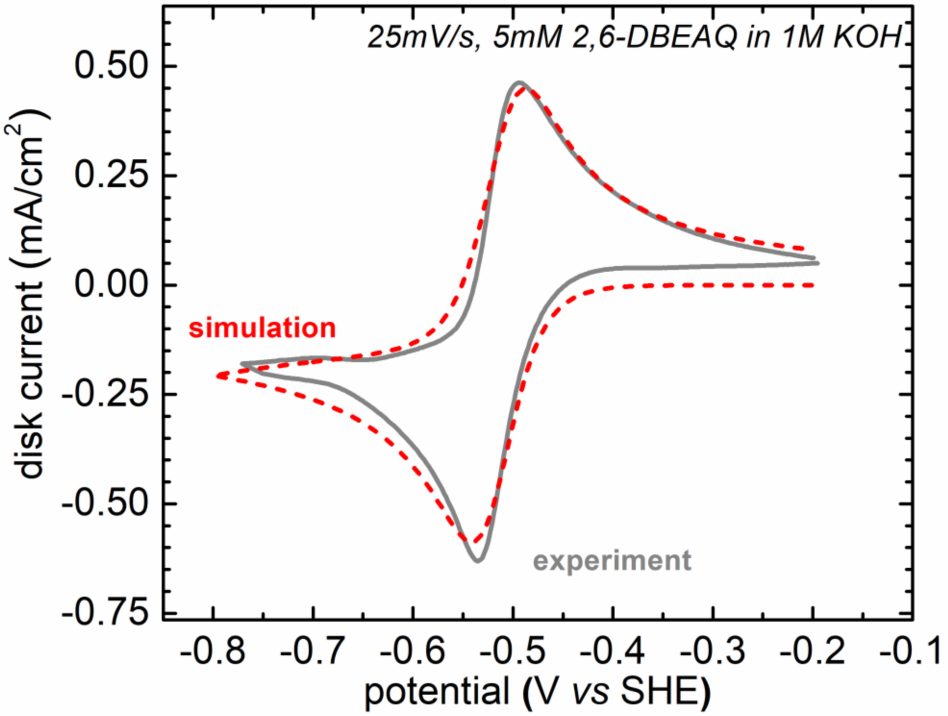

Figure S5. Capacitance-corrected CV of 5 mM 2,6-DBEAQ in 1 M KOH (solid grey line). The dashed red line represents the simulated total current arising from two successive one-electron reductions with reduction potentials of -0.517 and -0.511 V *vs* SHE, according to the procedure outlined in a previous publication. [1] Each simulated reduction has a rate constant $k_o = 7 \times 10^{-3}$ cm/s and α = 0.5. The diffusion coefficient of all redox states of 2,6-DBEAQ (oxidized, semiquinoid, and reduced) was assumed to be 1.58 × 10^{-6} cm^2/s (as obtained from the Levich plot in Figure S4).

Redox chemistry of 2,6-DBEAQ *vs* 2,6-DHAQ

Following our previous study on 2,6-DHAQ [1] and literature reports [2,3] on quinone electrochemistry in the absence of proton donors, we simulated the CV of 2,6-DBEAQ as representing two reversible electron transfer steps at two different potentials E_1 and E_2. The separation between simulated redox potentials for the first (E_1) and second (E_2) electron reductions for 2,6-DBEAQ is considerably narrower than the corresponding peak separation for 2,6-DHAQ [1] (6 mV *vs* 60 mV). An important implication of this difference is that there is a smaller driving force for the formation of semiquinone radicals between fully oxidized and fully reduced 2,6-DBEAQ species than there is for 2,6-DHAQ. In order to demonstrate why this is the case, we first explain the effect of E_1-E_2 separation on the reduction mechanism and then draw a connection between the reduction potential difference and the semiquinone concentration.

The pH dependence of the proton-coupled electron transfer (PCET) redox reaction for a generalized anthraquinone (AQ) is often visualized by the nine-membered square scheme (Figure S6). The horizontal direction indicates electron transfer (ET), and the vertical direction indicates proton transfer (PT or protonation). Under strongly alkaline conditions, where the pH is higher than the second pKa (pKa_2) of the reduced AQ (AQ^{2-}), no protonation of the semiquinone anion will take place, and reduction proceeds *via* two ET steps, from AQ to a semiquinone ($AQ^{-\bullet}$) at E_1, and from $AQ^{-\bullet}$ to AQ^{2-} at E_2 which is typically < E_1. Depending on the value of E_1–E_2, the mechanism of AQ reduction in alkaline conditions can either be a concerted one-step, two-electron process or two single-electron processes. When E_2 becomes more negative relative to E_1, a stepwise process via a semiquinone radical is followed, as in AQ reduction in aprotic solvents. [3,4] Under these conditions, a comproportionation reaction, where AQ and AQ^{2-} combine to generate $AQ^{-\bullet}$ semiquinone (Equation 3) is thermodynamically favorable. The equilibrium constant for this comproportionation (K_{eq_comp}) can be obtained by dividing the equilibrium constants of E_1 (Equation 4) by that of E_2 (Equation 5), which now becomes Equation 6.[2] The ratio between semiquinone concentration and the geometric mean of the concentrations of the oxidized and reduced forms of AQ can now be seen as an increasing function of E_1–E_2.

$$AQ \ + \ e^{-} \rightleftharpoons AQ^{-\cdot} \quad \text{(Eq 1)}$$

$$AQ^{-\cdot} \ + \ e^{-} \rightleftharpoons AQ^{2-} \quad \text{(Eq 2)}$$

$$AQ + AQ^{2-} \rightleftharpoons 2AQ^{-\cdot} \text{(Eq 3)}$$

$$E_1 = \frac{RT}{zF} lnK_{eq1};\ \boldsymbol{K_{eq1}} = \frac{[AQ^{-\cdot}]}{[AQ]} = exp\left(\frac{zF}{RT}E_1\right) \text{(Eq 4)}$$

$$E_2 = \frac{RT}{zF} lnK_{eq2};\ \boldsymbol{K_{eq2}} = \frac{[AQ^{2-}]}{[AQ^{-\cdot}]} = exp\left(\frac{zF}{RT}E_2\right) \text{(Eq 5)}$$

$$\boldsymbol{K_{eq\_comp}} = \frac{K_{eq1}}{K_{eq2}} = \frac{[AQ^{-\cdot}]^2}{[AQ]\cdot[AQ^{2-}]} = exp\left[\frac{zF}{RT}(E_1 - E_2)\right] \text{(Eq 6)}$$

This equation directly relates the concentration of semiquinone species to the E_1-E_2 separation and suggests that K_{eq_comp} for semiquinone formation is 2.83 times higher for 2,6-DHAQ than it is for 2,6-DBEAQ for the same AQ:AQ^{2-} ratio, based on their respective E_1-E_2 separations.

The differences in energy between the first and second reduction can also be estimated with electronic structure calculations. Conformers of the oxidized, one-electron reduced, and two-electron reduced forms of 2,6-DHAQ and 2,6-DBEAQ were generated with the UFF force field using RDKit.[5] The redox active sites of the one-electron and two-electron reduced forms were paired with one and two potassium cations, respectively. The deprotonated carboxyl and hydroxyl groups were also paired with potassium cations. This pairing is done to approximate the ion pairing behavior of the molecules in solution in lieu of an explicit solvent, as has been done previously.[6] The relative energies of the first and second reduction were calculated with both semi-empirical methods (PM7 COSMO) and density functional theory (DFT) methods in a polarizable continuum model (PCM) implicit solvent (B3LYP/6-311+G(d,p)). The DFT single point energies were evaluated at the B3LYP/6-31G(d) (no PCM) minima. Typically, when calculating reduction potentials, a calibration scheme is employed, [6] or the relative energetics of all molecules are computed relative to a fixed molecule where the experimental result is known;[4] the latter strategy is used in this case with 2-6 DHAQ used as the internal standard. We find that using DFT is necessary to qualitatively predict these differences (though the shift is overestimated) in the first and second reduction. This suggests that such a behavior can be screened for in future studies, at least for quantitative estimation of semiquinone presence.

Negolyte	B3LYP/6-311+G(d,p) PCM Estimated $E_1 - E_2$ (V)
2,6-DHAQ*	0.060
2,6-DBEAQ	-0.133

Table S3. Estimated difference in potential between the first and the second reduction for 2,6-DHAQ and 2,6-DBEAQ. *Note that the energy differences are calibrated so that the differences for 2,6-DHAQ are fixed to experiment.

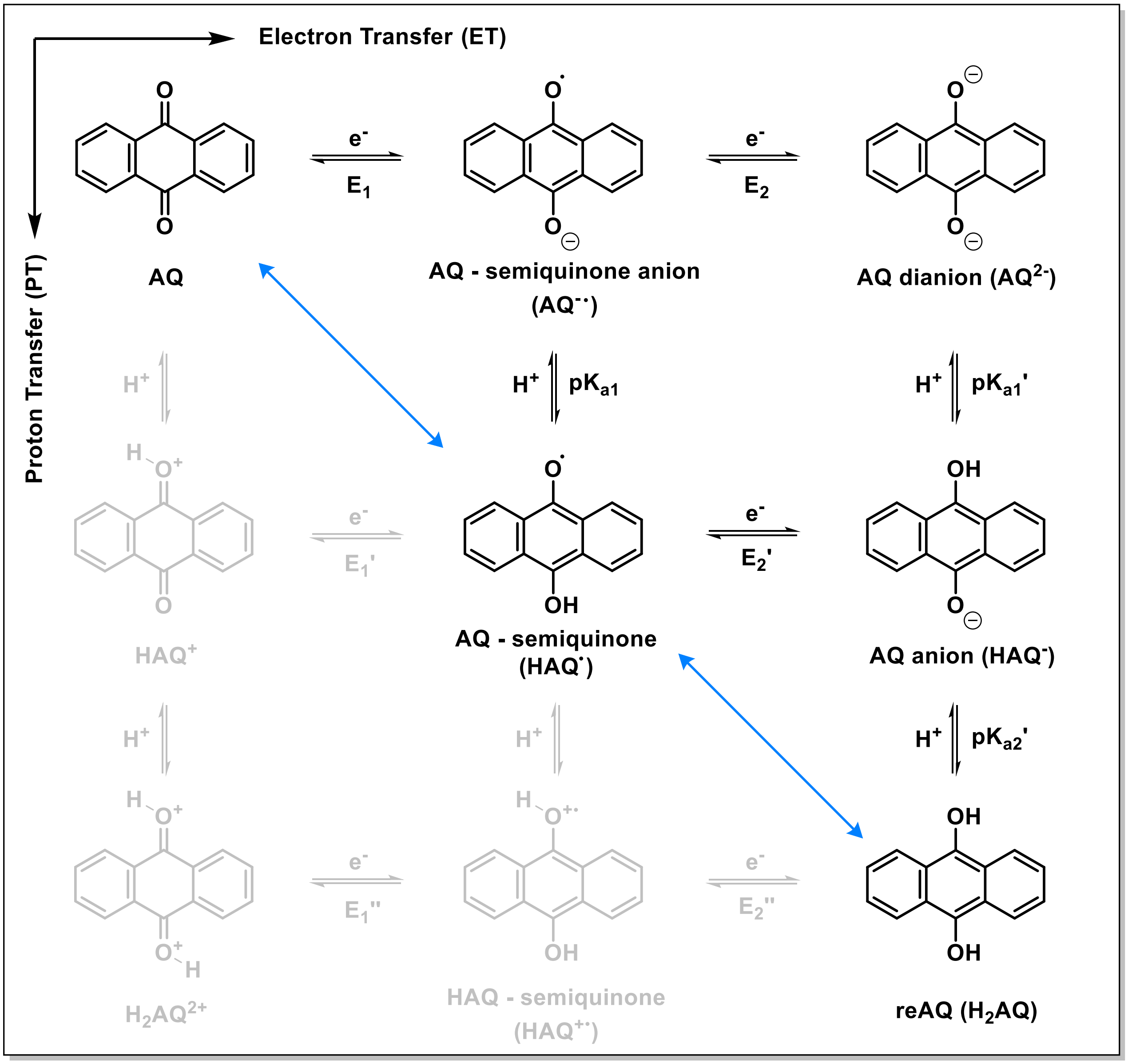

Figure S6. 9-membered Square Scheme of AQ Reduction. The horizontal direction indicates electron transfer onto the molecule at a given potential, i.e. E_1 and E_2, and the vertical direction indicates protonation of the species depending on the pKa of the generated anion and the solution pH. AQ states that are unstable under alkaline conditions are shown in grey. Blue arrows indicate PCET.

Theoretical calculations of DBEAQ isomer susceptibility to alkyl chain cleavage

The stability of disubstituted DBEAQ isomers against the loss of the alkyl groups was evaluated computationally. The first approach taken was to evaluate the relative reaction energies of the loss of the alkyl chain of both the oxidized and reduced forms of different isomers of DBEAQ. These reactions are shown in Scheme S1.

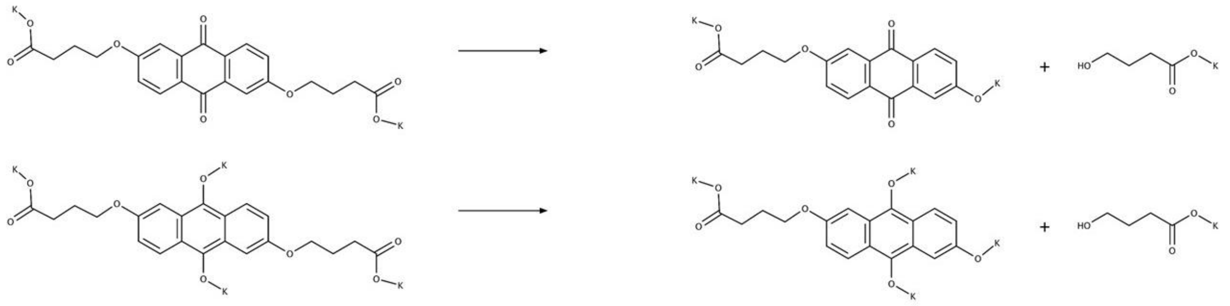

Scheme S1. Reaction energies evaluated to determine the relative thermodynamic stability of different isomers of DBEAQ in different oxidation states.

Optimizations were conducted at the PM7 level of theory with the COSMO solvation model using the MOPAC package.[7] Up to 20 conformers for each molecule were generated using RDKit.[5] Because the molecule is in alkaline conditions, the energies were evaluated for the deprotonated forms where explicit potassium cations are placed near the negative charges. The relative energies are shown in Table S4. Two important observations from these results are: (1) the reaction energies associated with chain loss are more thermodynamically favorable for the oxidized form in all cases, except in 2,6-DBEAQ, where the reduced form is slightly more susceptible. Second, the thermodynamic stability of both the oxidized and reduced forms of 2,6-DBEAQ are among the highest of all the isomers examined.

	Thermodynamic Loss of Chain (eV)		Reaction Energy to form Tetrahedral Intermediate (eV)
DBEAQ Chain Positions	Oxidized Form[a,b]	Reduced Form[a,b]	From Oxidized Form[a,c]
2,6	0.00	-0.06	0.00
1,2	-0.38	-0.19	-0.21
1,3	-0.27	-0.09	-0.38
1,4	-0.33	0.03	-0.20
1,5	-0.32	-0.13	-0.35
1,6	-0.35	0.00	-0.29
1,7	-0.56	-0.21	-0.21
1,8	-0.34	0.02	-0.27
2,3	-0.30	0.71	-0.21
2,7	0.00	0.86	-0.04

Table S4. Relative Energies of DBEAQ. [a] Energies calculated at the PM7 level of theory with the COSMO solvation model [b] Reaction energies are tabulated relative to the energy of 2,6-DBEAQ losing an alkyl chain in its oxidized form [c] Reaction energies to form tetrahedral intermediate are relative to the reaction energy for the oxidized form of 2,6-DBEAQ to form a tetrahedral intermediate.

Because the relative stability of the reduced form over the oxidized form cannot be completely explained by looking at only the thermodynamics of the final products, we investigated the thermodynamic landscape of possible intermediates. As the oxidized form is more electron deficient, we estimate the susceptibility to chain loss by evaluating the energy of a hydroxide-substituted intermediate of the DBEAQ molecule (Scheme S2). This intermediate should more easily form for the oxidized form. As done previously with bromination of anthraquinones,[8] the energy is estimated by evaluating the relative energy of the tetrahedral intermediate to that of the oxidized molecule (right-most column of Table S4). Here, we see that 2,6-DBEAQ is the most stable isomer, whereas 1,2- and 1,8-DBEAQ are less stable than 2,6-DBEAQ, which is consistent with experimental observation. Based on these findings, it appears that DBEAQ stability against alkyl chain loss is highly sensitive to the exact positioning of the two alkyl chains, particularly with respect to the ketone groups on the anthraquinone core.

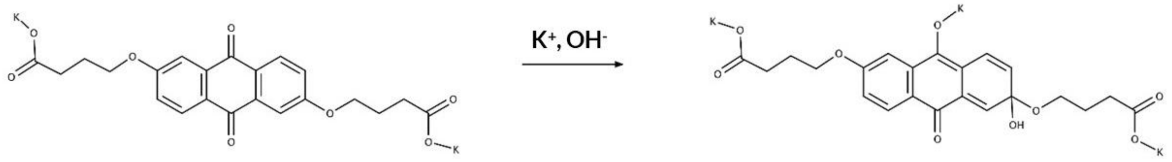

Scheme S2. Reaction of OH^- with oxidized form to form tetrahedral intermediate. Used as a means of estimating the vulnerability of the oxidized form to decomposition.

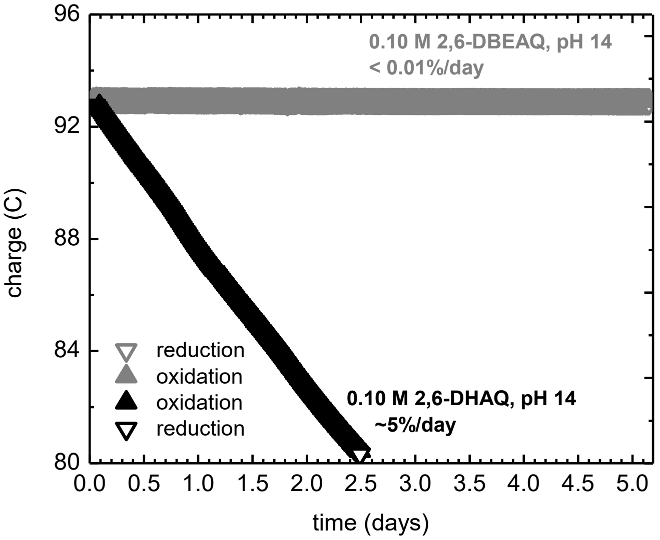

Figure S7. Unbalanced compositionally-symmetric cell cycling of 0.10 M 2,6-DBEAQ and 2,6-DHAQ, showing capacity *vs* time, both in 1 M KOH (pH 14). The capacity-limiting side was 5 mL 0.1 M 2,6-DBEAQ or DHAQ, while the non-capacity-limiting side was 10 mL of the same. Capacities were obtained by full potentiostatic reduction and oxidation of 5 mL of capacity-limiting side; potential was switched between ±0.2 V when magnitude of current dropped to 2 mA/cm^2. Cell cycle period is ~ 20 min.

Identification of a chemical decomposition pathway of 2,6-DBEAQ

Chemical stability studies performed at 75°C, 0.1 M concentration, and pH 14 indicate that the oxidized form of 2,6-DBEAQ is susceptible to decomposition (Figure S8). Samples of 2,6-DBEAQ were stored in the oxidized form at 0.1 M concentration in pH 14 aqueous solution (1 M KOH) in FEP vials in an oven at 75°C for 8 days. Decomposition peaks were observed in the ^{1}H NMR spectra (Figure S8c). Samples of 2,6-DBEAQ that were electrochemically reduced and treated under identical conditions exhibit no evidence of decomposition (Figure S8b).

We have identified that γ-hydroxybutyrate cleavage is involved in the decomposition of the oxidized form of 2,6-DBEAQ (Figure S9). The aliphatic region of the ^{1}H NMR spectrum of 2,6-DBEAQ treated at 75°C for 8 days at 0.1 M concentration in pH 14 aqueous solution (1 M KOH) in the oxidized form (Figure S9c) was compared to that of γ-butyrolactone (Sigma Aldrich) prepared in a pH 14 aqueous solution (1 M KOD in D_2O with 10 mM $NaCH_3SO_3$ internal standard) (Figure S9b), as γ-butyrolactone hydrolyzes to its acyclic form, γ-hydroxybutyrate, under basic conditions. The spectrum of 2,6-DBEAQ treated at 75°C (Figure S9c) includes protons D, E, and F, corresponding to the 2,6-DBEAQ aliphatic protons (Figure S9a); protons D´´, E´´, and F´´, corresponding to those of γ-hydroxybutyrate (Figure S9b); and protons D´, E´, and F´, corresponding to the aliphatic protons of the monoalkylated decomposition product (4-((6-oxido-9,10-dioxo-9,10-dihydroanthracen-2-yl)oxy)butanoate) after the cleavage of γ-hydroxybutyrate. The spectrum of 2,6-DBEAQ treated at 75°C with 10 mM (0.5 µL) γ-hydroxybutyrate added to the NMR sample (Figure S9d) exhibits an increase in the size of the peaks corresponding to protons D´´, E´´, and F´´, verifying the involvement of γ-hydroxybutyrate cleavage in the decomposition of the oxidized form of 2,6-DBEAQ. The relative peak integrals of the spectra of 2,6-DBEAQ treated at 75°C are also consistent with the products of γ-hydroxybutyrate cleavage. This decomposition pathway for the oxidized form of 2,6-DBEAQ, along with the stability of the relatively more electron-rich reduced form of 2,6-DBEAQ, is consistent with a nucleophilic hydroxide-mediated decomposition mechanism. As we observe that the monoalkylated decomposition product further decomposes into 2,6-DHAQ via cleavage of a second γ-hydroxybutyrate moiety, the by-products of γ-hydroxybutyrate cleavage may be susceptible to further decomposition leading to corresponding capacity fade, as previously observed in 2,6-DHAQ (Figure S7).

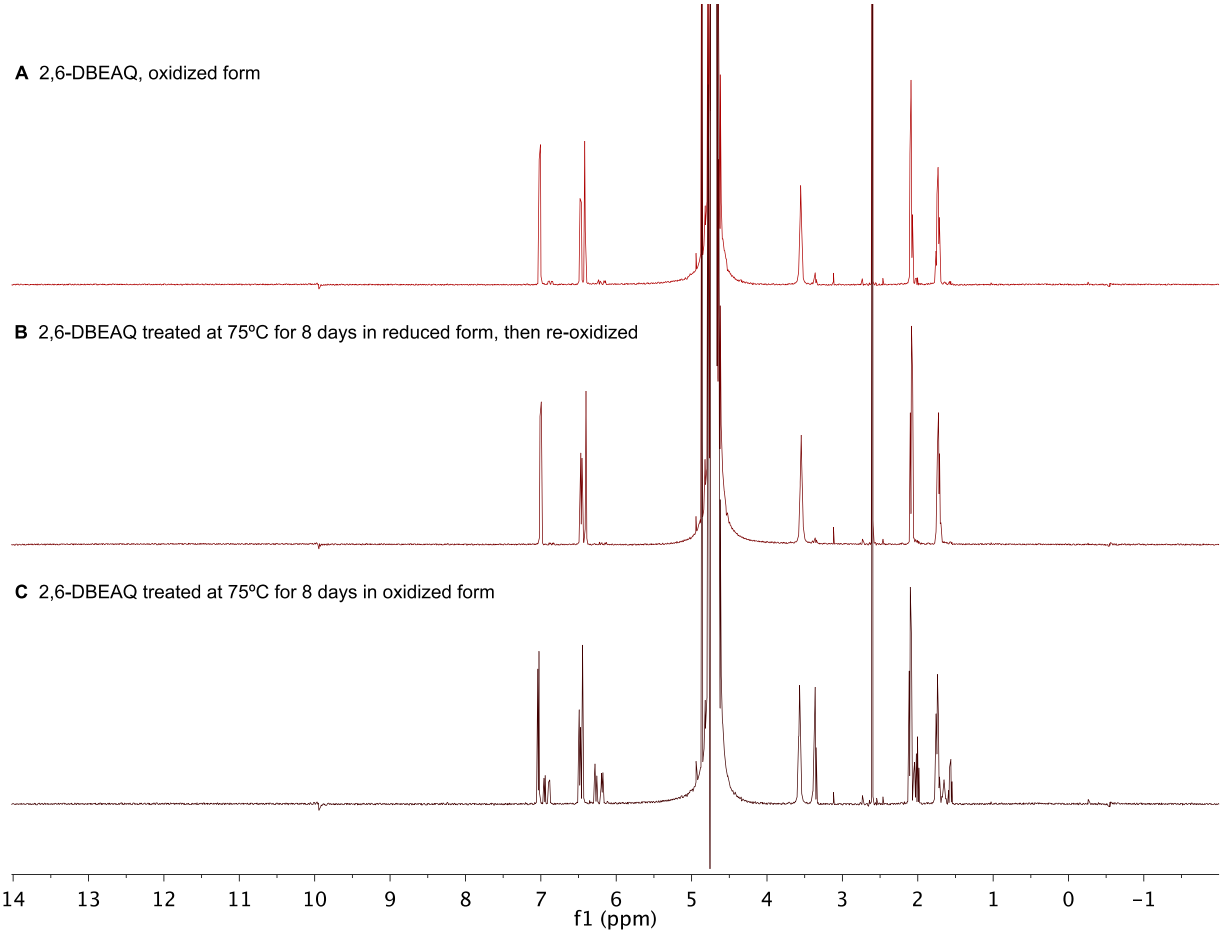

Figure S8. NMR evidence of decomposition of 2,6-DBEAQ in the oxidized form. ^{1}H NMR spectra (500 MHz, 1 M KOD in D_2O with 10 mM $NaCH_3SO_3$ internal standard) of (a) the oxidized form of 2,6-DBEAQ in pH 14 aqueous solution (1 M KOH); (b) 2,6-DBEAQ treated at 75°C for 8 days at 0.1 M concentration in pH 14 aqueous solution (1 M KOH) in the reduced form and then re-oxidized in order to compare to samples tested in the oxidized form; (c) 2,6-DBEAQ treated at 75°C for 8 days at 0.1 M concentration in pH 14 aqueous solution (1 M KOH) in the oxidized form.

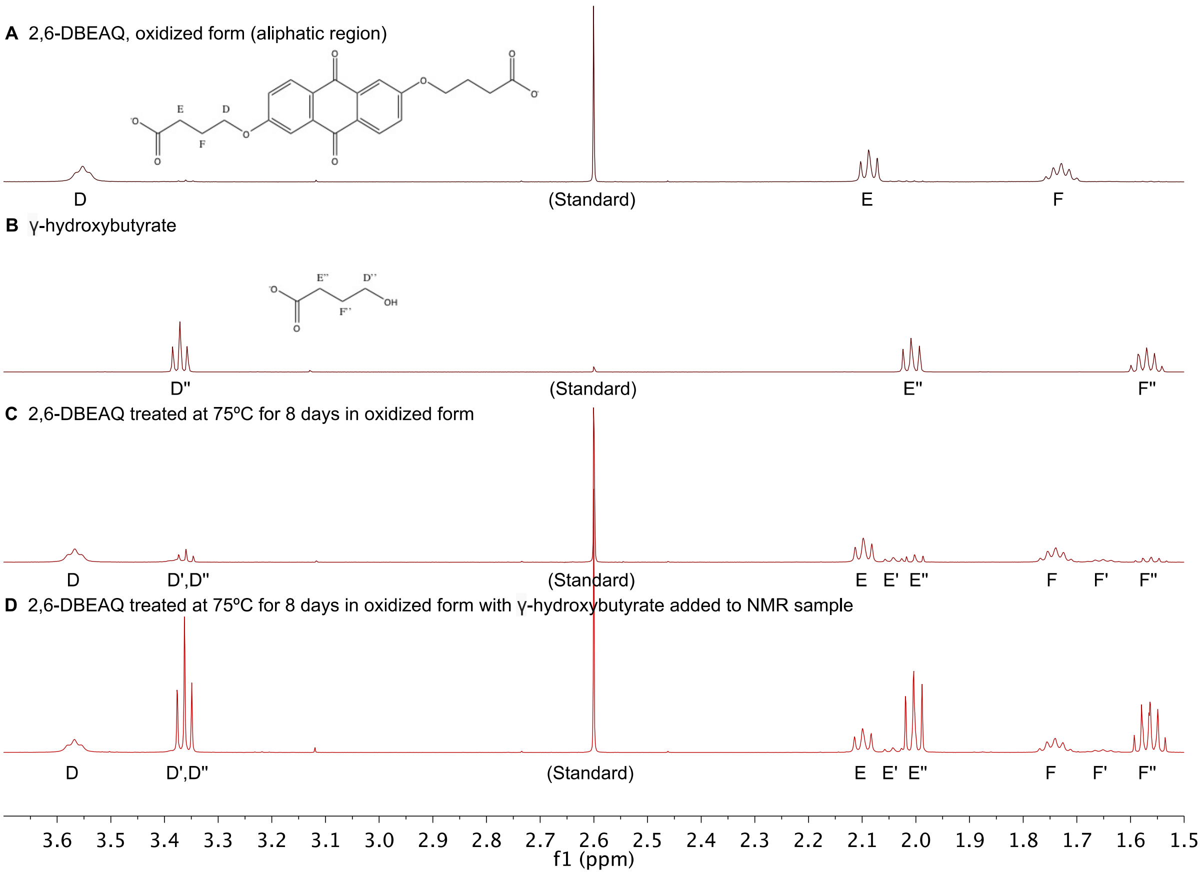

Figure S9. Identification of a decomposition product of 2,6-DBEAQ. ^{1}H NMR spectra (500 MHz, 1 M KOD in D_2O with 10 mM $NaCH_3SO_3$ internal standard) of (a) aliphatic region of the oxidized form of 2,6-DBEAQ in pH 14 aqueous solution (1 M KOH); (b) γ-hydroxybutyrate; (c) aliphatic region of 2,6-DBEAQ treated at 75°C for 8 days at 0.1 M concentration in pH 14 aqueous solution (1 M KOH) in the oxidized form; (d) aliphatic region of 2,6-DBEAQ treated at 75°C for 8 days at 0.1 M concentration in pH 14 aqueous solution (1 M KOH) in the oxidized form with 10 mM γ-hydroxybutyrate added to the NMR sample.

Characterization of the time course of γ-hydroxybutyrate cleavage

Further chemical stability studies were performed to characterize the time course of γ-hydroxybutyrate cleavage of 2,6-DBEAQ. Samples of 2,6-DBEAQ in the oxidized form at 0.1 M and 0.5 M concentrations in deuterated aqueous solutions at pH 12 and pH 14 were stored in sealed 5 mm Precision Low Pressure/Vacuum Valve (LPV) NMR sample tubes (Wilmad-LabGlass Product No. 535-LPV-7), lined with 5 mm FEP tube liners (Wilmad-LabGlass Product No. 6005-8) to prevent etching of the NMR tubes under alkaline conditions. The samples were heated in ovens at 65°C and 95°C for a period of several weeks, during which reaction progress was monitored by NMR. Two equivalent samples were prepared and tested for each condition. Sealed LPV NMR tubes were used to prevent the escape of water vapor from the sample tubes during heating. pH 14 solutions were prepared by dissolving 2,6-DBEAQ in D_2O with the concentration of KOD required to fully deprotonate the molecule plus an additional 1 M KOD (2 M KOD for 0.5 M 2,6-DBEAQ and 1.2 M KOD for 0.1 M 2,6-DBEAQ). pH 12 solutions were prepared by dissolving 2,6-DBEAQ in D_2O with the concentration of KOD required to fully deprotonate the molecule plus an additional

10 mM KOD (1.01 M KOD for 0.5 M 2,6-DBEAQ and 0.21 M KOD for 0.1 M 2,6-DBEAQ), with additional KOD added as necessary until pH 12 was reached, as measured by a pH meter (Oakton WD-35419-12 pH 700 Benchtop Meter, Oakton WD-35805-06 pH electrode). The fraction of 2,6-DBEAQ remaining in each sample was measured at intervals as the ratio of the total integral of the aromatic ^{1}H peaks of 2,6-DBEAQ to the total integral of all aromatic ^{1}H peaks in the sample. To perform this analysis on samples at 0.5 M concentration, in which ^{1}H peaks overlap due to peak broadening, deconvolution was performed using the line fitting feature in MestReNova to obtain ^{1}H peak integrals. To ensure that the ratio of aromatic ^{1}H peaks of 2,6-DBEAQ to the total integral of all aromatic ^{1}H peaks corresponds to the concentration of 2,6-DBEAQ remaining in a sample relative to the initial 2,6-DBEAQ concentration, the integral of one ^{1}H peak of 2,6-DBEAQ was measured relative to that of an internal standard (0.1 M $NaCH_3SO_3$ in D_2O). The internal standard solution was prepared in a sealed capillary tube that was inserted in each NMR tube before a measurement was taken and removed from the sample during heating to prevent decomposition of and reactions with the internal standard. NMR tubes were cooled in a water bath before the valve was removed to insert the capillary tube to prevent the escape of water vapor from the sample tubes. Good agreement was found between both methods of tracking the time course of 2,6-DBEAQ decomposition, confirming that the ratio of aromatic ^{1}H peaks of 2,6-DBEAQ to the total integral of all aromatic ^{1}H peaks could be used as a measure of reaction progress.

Figure S10 illustrates the time course of 2,6-DBEAQ decomposition for samples treated at 65°C and 95°C, at pH 12 and pH 14, and at 0.1 M and 0.5 M concentration in the oxidized form. Error bars correspond to the standard deviation of measurements obtained from equivalent samples. Samples of 2,6-DBEAQ that were electrochemically reduced and stored for 13 days in sealed FEP-lined LPV NMR tubes at the same temperature, pH, and concentration conditions as those reported here for the oxidized form exhibit less than 10% decomposition in all conditions and less than 5% decomposition in all except the 95°C, pH 12, 0.5 M condition.

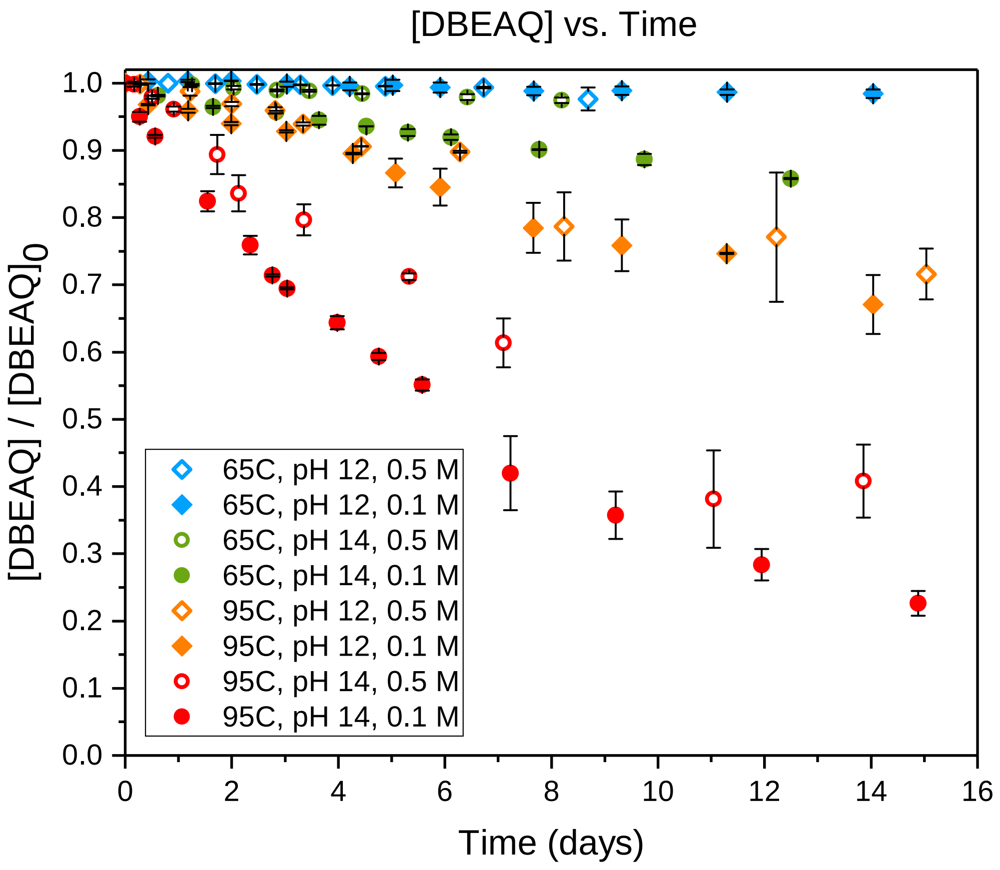

Figure S10. Time course of 2,6-DBEAQ decomposition at various temperature, pH, and concentration conditions. The remaining concentration of 2,6-DBEAQ relative to the initial concentration *vs* time (in days) for samples treated at 65°C and 95°C, at pH 12 and pH 14, and at 0.1 M and 0.5 M concentration in the oxidized form. Error bars correspond to the standard deviation of measurements obtained from equivalent samples.

For samples at pH 14 and at 0.1 M 2,6-DBEAQ concentration (in which the concentration of hydroxide ions exceeds that of 2,6-DBEAQ by tenfold so a pseudo reaction order with respect to 2,6-DBEAQ may be inferred), the linear fit of the semi-logarithmic plot of 2,6-DBEAQ concentration *vs* time, shown in Figure S11a for the 95°C condition, is consistent with pseudo-first order reaction kinetics with respect to 2,6-DBEAQ ($R^2 = 0.994$ for the 95°C condition, $R^2 = 0.987$ for the 65°C condition). Comparison of the semi-logarithmic plot (Figure S11a) to the same data plotted on a linear scale (Figure S11b, $R^2 = 0.919$) and as the reciprocal of 2,6-DBEAQ concentration *vs* time (Figure S11c, $R^2 = 0.968$) confirms the inference of pseudo-first order kinetics rather than pseudo-zero order or pseudo-second order kinetics with respect to 2,6-DBEAQ. The corresponding effective (pseudo-first order) rate constants are 0.10 days^{-1} at 95°C and 0.012 days^{-1} at 65°C. The corresponding activation energy estimated from the Arrhenius equation is 70 kJ/mol (20 kcal/mol). The effective rate constant extrapolated to 25°C is 0.0004 days^{-1}, corresponding to a room temperature half-life on the order of 5 years for decomposition of the oxidized form of 2,6-DBEAQ at pH 14 and at 0.1 M concentration. In the parameter space studied (Figure S10), we report slower decomposition at pH 12 relative to pH 14 and slower decomposition at 0.5 M relative to 0.1 M concentration. We also report substantially slower decomposition of the reduced form relative to the oxidized form of 2,6-DBEAQ.

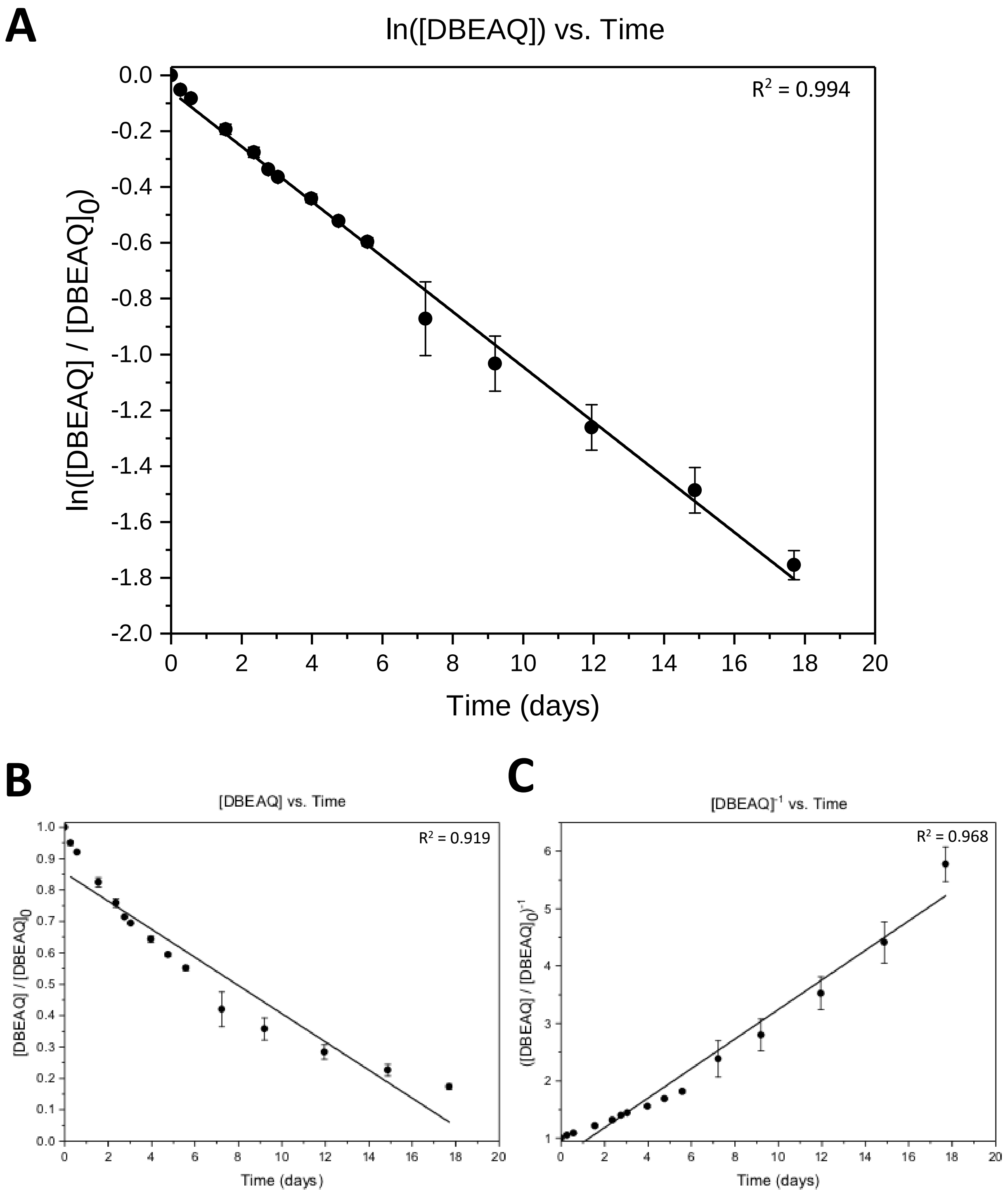

Figure S11. Evidence of pseudo-first order decomposition kinetics with respect to 2,6-DBEAQ. The remaining concentration of 2,6-DBEAQ relative to the initial concentration *vs* time (in days) for samples treated at 95°C, at pH 14, and at 0.1 M concentration in the oxidized form, plotted (a) on a semi-logarithmic scale; (b) on a linear scale; (c) as the reciprocal of the 2,6-DBEAQ concentration relative to the initial concentration *vs* time. Error bars correspond to the standard deviation of measurements obtained from equivalent samples.

A note on DBEAQ/DHAQ permeability

The permeability of the oxidized form of 2,6-DBEAQ (5.26×10^{-13} cm^2/s) in Fumasep E-600 series membrane (with ion exchange capacity of 1.70 meq/g) is about an order of magnitude lower than is typical for permeabilities of quinone-based molecules under alkaline conditions across more widely used commercial membranes (e.g. Nafion). Permeability of the oxidized form of 2,6-DBEAQ (with two negative charges) was measured because we expect it to have a higher permeability than the reduced form, which should cross over more slowly through the cation-exchange membrane owing to it having four negative charges instead of two.

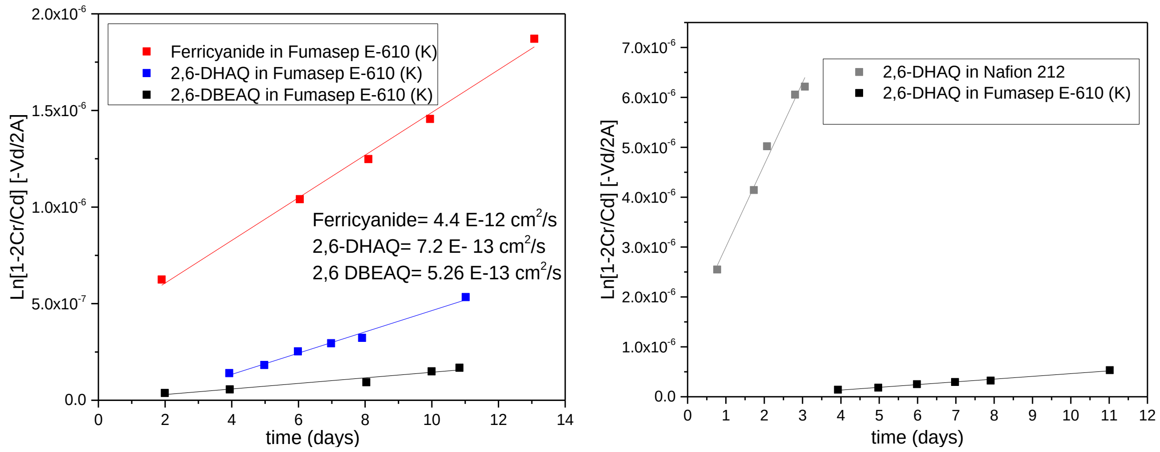

Figure S12. (a) The permeability of the oxidized form of 2,6-DBEAQ, 2,6-DHAQ, and potassium ferricyanide across a Fumasep E-610 (K) membrane. (b) 2,6-DHAQ in Nafion 212 and Fumasep E-610 (K). The slope represents the permeability.

We found that 2,6-DHAQ had a similarly low permeability across Fumasep E-610 (K) (10 μm, 7.24×10^{-13} cm^2/s), in contrast to Nafion 212 (50 μm, 1.39×10^{-11} cm^2/s).

These permeabilities imply that, assuming the membrane remains chemically stable, it would take at least 3,000 years for 2,6-DBEAQ/DHAQ permeation through Fumasep E-610 (K) to lead to a 50% loss in cell capacity; it would take 200 years for potassium ferricyanide permeation to lead to a similar loss, as it is the faster-crossing species. Fluoropolymer membranes for vanadium redox batteries comprise over 40% of the cost of the power stack and a significant fraction of the cost of the entire system.[9] The anticipated cost for Fumasep E-620 (K) (20 μm) at large production scale is < \$25/m^2, which is more than an order of magnitude less expensive than fluoropolymers (Bernd Bauer, private communication, March 17, 2018).

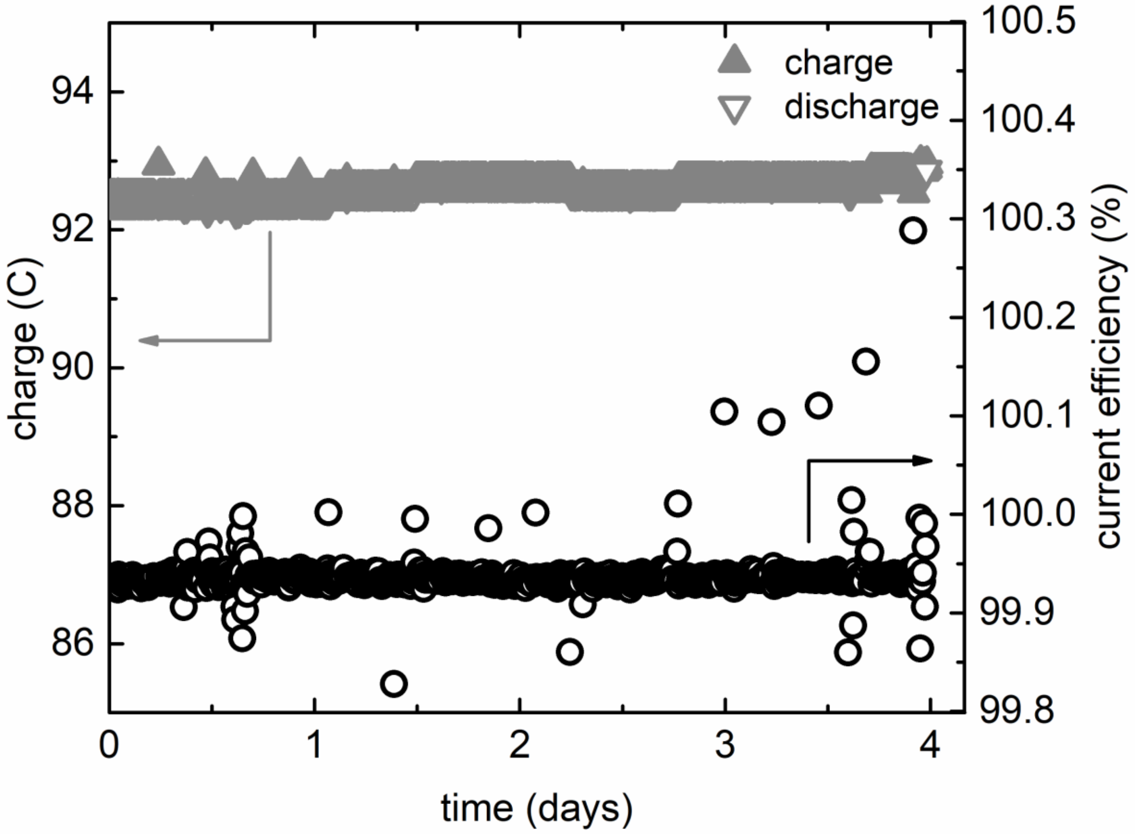

Figure S13. Capacity and current efficiency (capacity on discharge divided by the capacity of the preceding charge step) as functions of time during galvanostatic cycling of a cell with a negolyte of 5.5 mL 0.1 M 2,6-DBEAQ and posolyte of 15 mL 0.20 M potassium ferrocyanide and 0.08 M potassium ferricyanide, both at pH 14 (880 cycles with each cycle 6.5 minutes long). Galvanostatic cycling was performed at 100 mA/cm^2 with voltage cutoffs of 1.4 and 0.6 V on charge and discharge, respectively.

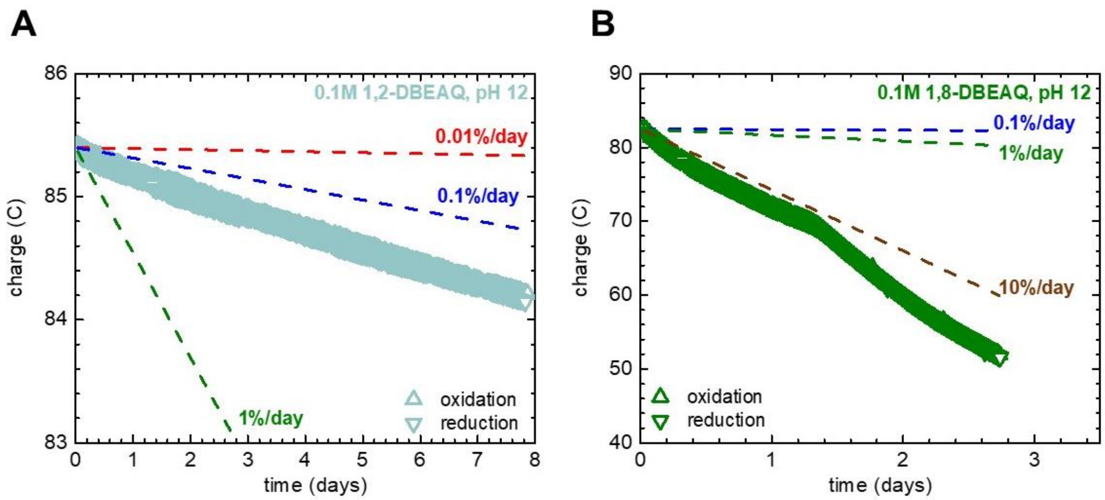

Figure S14. Unbalanced compositionally-symmetric cell cycling of 0.10 M (a) 1,2- and (b) 1,8-DBEAQ, showing capacity *vs* time, both in 0.01 M KOH (pH 12). The capacity-limiting side was 5 mL 0.1 M DBEAQ, while the non-capacity-limiting side was 10 mL of the same. Capacities were obtained by full potentiostatic reduction and oxidation of 5 mL of capacity-limiting side; potential was switched between ±0.2 V when magnitude of current dropped to 2 mA/cm^2. Linear fits between 0.01 and 10 %/day are drawn to compare against experimental data.

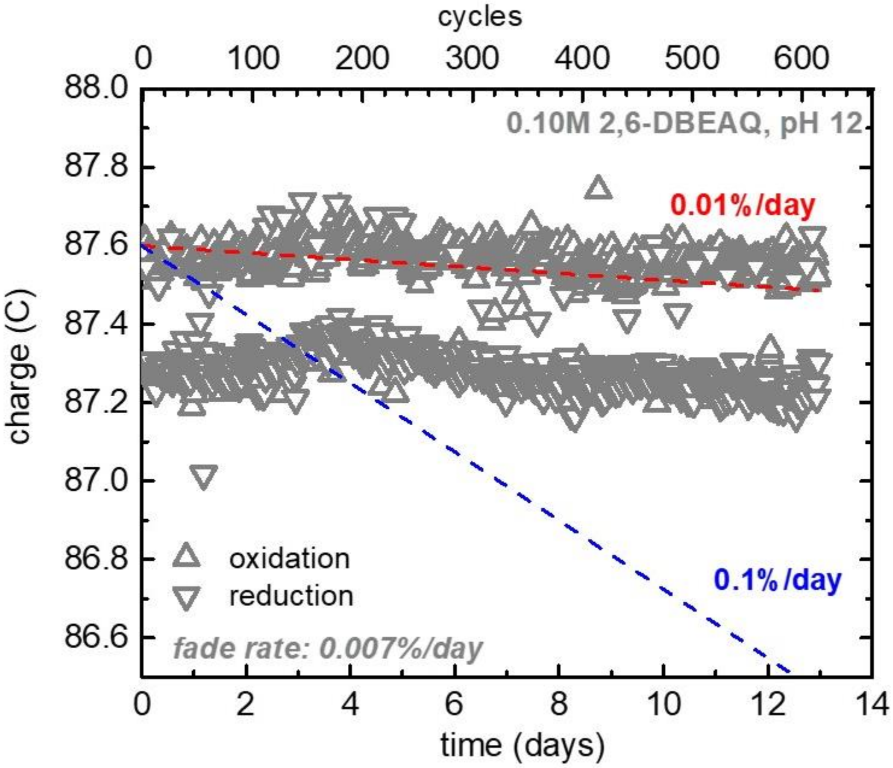

Figure S15. Unbalanced compositionally-symmetric cell cycling of 0.10 M 2,6-DBEAQ, showing capacity *vs* time in 0.01 M KOH (pH 12). The capacity-limiting side was 5 mL 0.1 M 2,6-DBEAQ, while the non-capacity-limiting side was 10 mL of the same. Capacities were obtained by full potentiostatic reduction and oxidation of 5 mL of capacity-limiting side; potential was switched between ±0.2 V when magnitude of current dropped to 2 mA/cm^2. Dashed lines with slopes of 0.01 and 0.1 %/day are drawn to compare against experimental data, which showed a temporal fade rate of approximately 0.007 %/day.

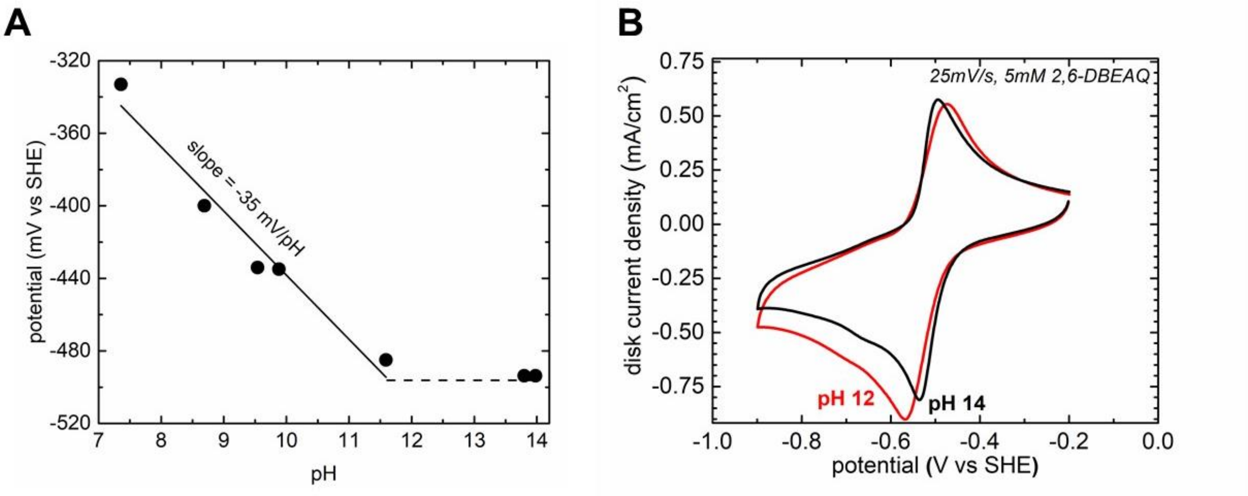

Figure S16. (a) Pourbaix diagram of 2,6-DBEAQ with a slope fit to the data of -35 mV/pH below pH 12. Above pH ~ 11.5, the potential is pH-independent, indicating that both oxidized and reduced forms of 2,6-DBEAQ are deprotonated. The dashed line has zero slope. (b) Capacitance-corrected CVs of 5 mM 2,6-DBEAQ in 1 M KOH (black curve) and pH 12 buffer (red curve) solution. We hypothesize the wider peak separation in the buffered pH 12 solution to be a result of slower kinetics for the first and second electron reduction steps[3] rather than a larger difference between their redox potentials.

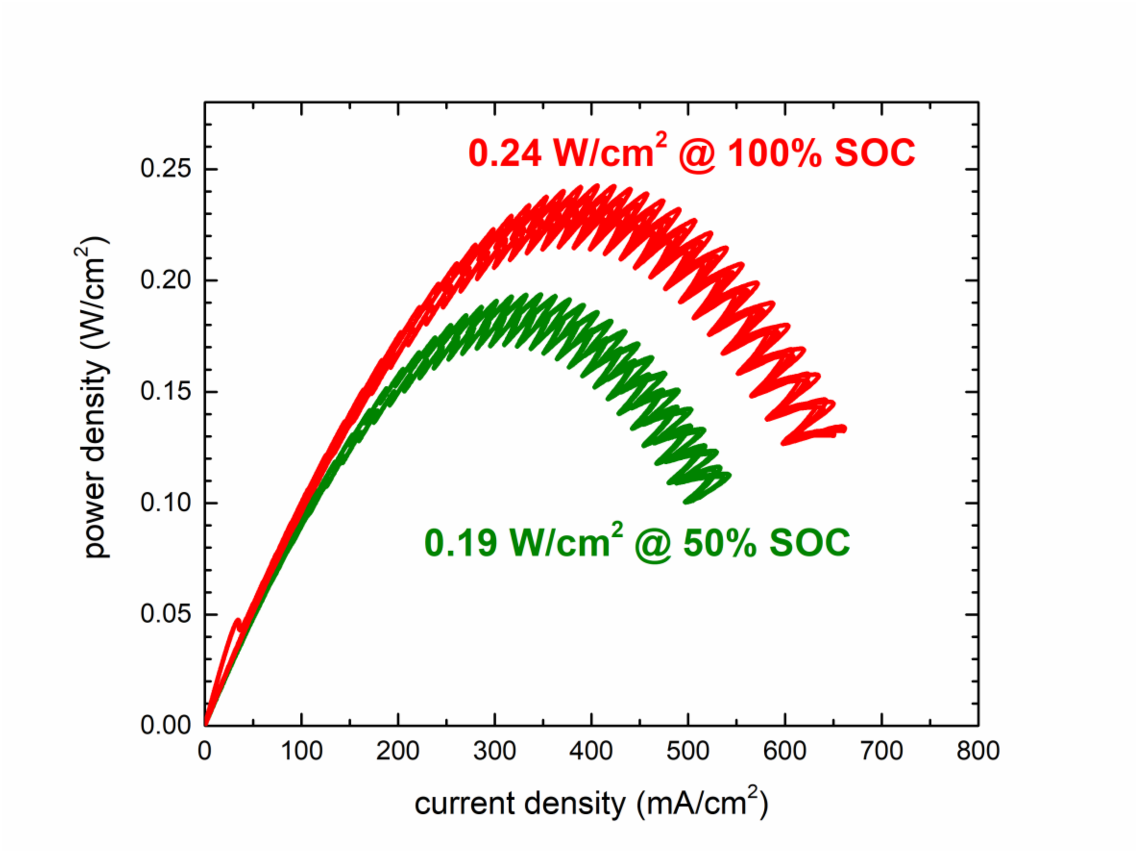

Figure S17. Power density *vs* current density for 0.5 M 2,6-DBEAQ at 20°C at 50% and ~100% SOC.

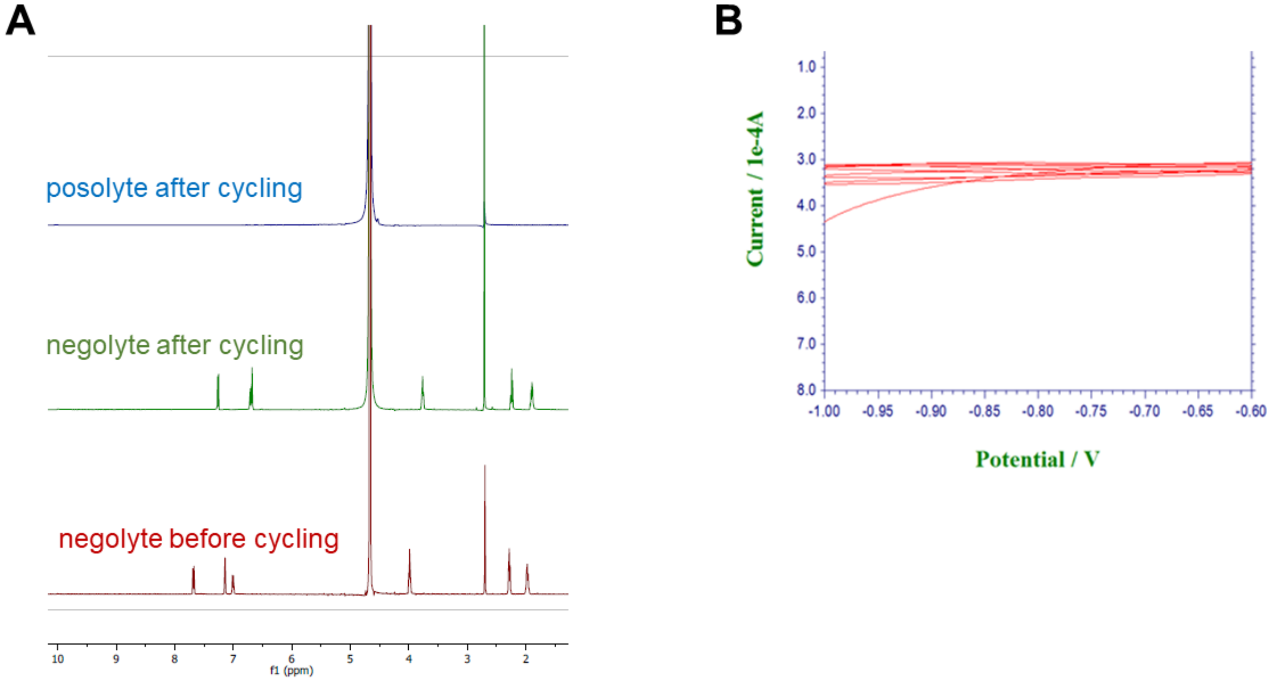

Figure S18. (a) NMR analysis of electrolytes from a cell compositionally similar to that in Figure 4a and cycled for 11 days. The origin of the peak shifts in NMR is unknown but could stem from differences slight differences in pH. (b) CV measurement of cycled posolyte showing no 2,6-DBEAQ redox peaks within the potential window (*vs* Ag/AgCl).

Estimated cost of electrolytes

The U.S. Department of Energy has a cost target of $150/kWh for the entire storage system. The current price for vanadium pentoxide (98% pure) is $15.15/lb. (www.vanadiumprice.com accessed 6/15/2018), which equates to $160/kWh for both electrolytes of a 1.45-volt all-vanadium flow battery. To this, one should add the cost of purification, but we do not do so here.

The mass-production cost of 2,6-DBEAQ, a new composition of matter, is not known at present, but cost projections for similar anthraquinones DHAQ (Fig. S1 of ref. [10]) and AQDS (ref. [11]) were recently reported to be between $0.92/kg and $3.92/kg when manufactured in the quantities necessary for GWh storage. (We note that the world's largest battery, the Rongke Power vanadium redox flow battery under construction near Dalian, China, is to have a capacity of 3.2 GWh.) The similarity of 2,6-DBEAQ to, and its synthesis from, 2,6-DHAQ make it plausible that its cost will not be much greater than that of DHAQ. Before we can perform a similar estimate of the cost of 2,6-DBEAQ *vs* scale, an industrially-compatible synthesis method must be developed with attributes such as high yield, and then the process analyzed for cost. Until then, we use $0.92/kg - $3.92/kg as an estimate of the cost range for anthraquinones at large scale, resulting in between $7/kWh and $29/kWh for the 2-electron-accepting DBEAQ in the negolyte.

A recent paper by Yuan et al. [12] quotes the cost of sodium ferrocyanide at \$1.07/kg. Although we used potassium ferrocyanide in our system, we do not expect this to cost much more than twice the price of the sodium form based on similar comparisons from the same source (from Yuan *et al.*, NaOH costs \$0.4/kg, whereas KOH costs \$0.84/kg). Hence, we estimate a cost of roughly \$2.15/kg for potassium ferrocyanide, amounting to \$32/kWh for the posolyte in our 1.05 V battery. Therefore, at large scale, we expect the combined cost of our electrolytes to be between \$39/kWh and \$61/kWh. To the extent that we are able to mix Na^+ with K^+ in the electrolyte, as discussed above to raise solubility, the cost of chemicals will be further decreased.

Supplemental References

[1] K. Lin, Q. Chen, M.R. Gerhardt, L. Tong, S.B. Kim, L. Eisenach, A.W. Valle, D. Hardee, R.G. Gordon, M.J. Aziz, and M.P. Marshak, "Alkaline Quinone Flow Battery", *Science* **349**, 1529 (2015).

[2] C. Costentin, "Electrochemical Approach to the Mechanistic Study of Proton-Coupled Electron Transfer", *Chem. Rev.* **108**, 2145 (2008).

[3] M. Quan, D. Sanchez, M.F. Wasylkiw, and D.K. Smith, "Voltammetry of Quinones in Unbuffered Aqueous Solution: Reassessing the Roles of Proton Transfer and Hydrogen Bonding in the Aqueous Electrochemistry of Quinones", *Journal of American Chemical Society* **129**, 12847 (2007).

[4] M.T. Huynh, C.W. Anson, A.C. Cavell, S.S. Stahl, and S. Hammes-Schiffer, "Quinone 1 e- and 2 e-/2 H+ Reduction Potentials: Identification and Analysis of Deviations from Systematic Scaling Relationships", *J Am Chem Soc* **138**, 15903 (2016).

[5] Rdkit: Open Source Cheminformatic Software (http://www.rdkit.org/).

[6] S. Er, C. Suh, M.P. Marshak, and A. Aspuru-Guzik, "Computational Design of Molecules for an All-Quinone Redox Flow Battery", *Chem. Sci.* **6**, 885 (2015).

[7] J.J.P. Stewart, Mopac2016, Version: 17.173l.

[8] M.R. Gerhardt, L. Tong, R. Gómez-Bombarelli, Q. Chen, M.P. Marshak, C.J. Galvin, A. Aspuru-Guzik, R.G. Gordon, and M.J. Aziz, "Anthraquinone Derivatives in Aqueous Flow Batteries", *Advanced Energy Materials* 1601488 (2017).

[9] S. Eckroad, "Vanadium Redox Flow Batteries: An in-Depth Analysis (#1014836)," Electric Power Research Institute, 2007.

[10] Z. Yang, L. Tong, D.P. Tabor, E.S. Beh, M.-A. Goulet, D. De Porcellinis, A. Aspuru-Guzik, R.G. Gordon, and M.J. Aziz, "Alkaline Benzoquinone Aqueous Flow Battery for Large-Scale Storage of Electrical Energy", *Advanced Energy Materials* **7**, 1702056 (2017).

[11] V. Dieterich, J. Milshtein, J. Barton, T. Carney, R. Darling, and F. Brushett, "Estimating the Cost of Organic Battery Active Materials: A Case Study on Anthraquinone Disulfonic Acid", *Translational Materials Research* **in press**, (2018).

[12] Z. Yuan, Y. Duan, T. Liu, H. Zhang, and X. Li, "Toward a Low Cost Alkaline Zinc-Iron Flow Battery with a Polybenzimidazole Custom Membrane for Stationary Energy Storage", *iScience* (2018. DOI: 10.1016/j.isci.2018.04.006).